Measurement of $W^{\pm}$ and Z Boson Production Cross Sections in pp Collisions at $\sqrt{s}$ = 13 TeV with the ATLAS Detector

The ATLAS Collaboration

Abstract

Measurements of the $W^{\pm} \rightarrow \ell^{\pm}\nu$ and $Z \rightarrow \ell^{+}\ell^{-}$ production cross sections (where $\ell^{\pm} = e^{\pm}, \mu^{\pm}$) in proton-proton collisions at $\sqrt{s}$ = 13 TeV are presented using data recorded by the ATLAS experiment at the LHC, corresponding to a total integrated luminosity of approximately 85 pb^{-1}. The total inclusive $W^{\pm}$ boson production cross sections times the single-lepton-flavour branching ratios are $\sigma_{W^+}^{\text{tot}}$ = [10960±20 (stat)±440 (sys)±990 (lumi)] pb and $\sigma_{W^-}^{\text{tot}}$ = [8380±20 (stat)±350 (sys)±750 (lumi)] pb for W^+ and W^- respectively. The total inclusive Z boson production cross section times leptonic branching ratio, within the invariant mass window $66 < m_{\ell\ell} < 116$ GeV, is σ_{Z}^{tot} = [1869±7 (stat)±42 (sys)±168 (lumi)] pb. The W^+, W^-, and Z boson production cross sections and cross-section ratios are also measured within a fiducial region defined by the detector acceptance. Theoretical predictions based on calculations accurate to NLO for electroweak and NNLO for QCD, using different PDF sets and predictions from different Monte Carlo generators, are compared to the measurements.

1 Introduction

The measurement of weak vector boson production at hadron colliders provides a benchmark of our understanding of quantum chromodynamic (QCD) and electroweak (EW) processes. The relatively large production cross sections and easily identifiable decays to leptonic final states offer a clean experimental signature which can be measured to high precision. In addition, theoretical predictions are available up to next-to-next-to-leading-order (NNLO) accuracy in QCD, and include EW corrections at next-to-leading-order (NLO) accuracy. The cross-section predictions are dependent on the parton distribution functions (PDFs) and are thus sensitive to the underlying dynamics of strongly interacting beam particles. Therefore, measurements of $W^\pm$ and Z boson[1] production offer a unique opportunity to test models of parton dynamics at the Large Hadron Collider's (LHC) new higher operating centre-of-mass energy of $\sqrt{s} = 13$ TeV.

This note details measurements by the ATLAS experiment of the total inclusive production cross sections times leptonic branching ratios for the $W \to e\nu$, $W \to \mu\nu$, $Z \to e^+e^-$, and $Z \to \mu^+\mu^-$ processes. The charge-specific cross sections for W^+ and W^- boson production are also presented. These measurements are used to evaluate cross-section ratios of W^+ to W^- production and of $W^\pm$ to Z production. All of the measurements are performed with pp collision data corresponding to an integrated luminosity of approximately 85 pb^{-1}, collected at $\sqrt{s} = 13$ TeV with the ATLAS detector during the Large Hadron Collider Run 2.

2 The ATLAS detector

The ATLAS experiment [1] is a multi-purpose particle detector with a forward-backward symmetric cylindrical geometry and nearly 4π coverage in solid angle.[2] The collision point is surrounded by inner tracking devices followed by a superconducting solenoid providing a 2 T magnetic field, a calorimeter system, and a muon spectrometer.

The inner tracker provides precision tracking of charged particles for pseudorapidities $|\eta| < 2.5$. It consists of pixel and silicon-microstrip detectors inside a transition radiation tracker. One significant upgrade for the new 13 TeV running period is the presence of the Insertable B-Layer [2], an additional pixel layer that provides high-resolution hits at small radius to improve tracking performance.

In the pseudorapidity region $|\eta| < 3.2$, high-granularity lead/liquid-argon (LAr) electromagnetic (EM) sampling calorimeters are used. An iron/scintillator tile calorimeter measures hadron energies for $|\eta| < 1.7$. The endcap and forward regions, spanning $1.5 < |\eta| < 4.9$, are instrumented with LAr calorimeters for both EM and hadronic measurements.

The muon spectrometer consists of three large superconducting toroids with 8 coils each, a system of trigger chambers, and precision tracking chambers, which provide triggering and tracking capabilities in the ranges $|\eta| < 2.4$ and $|\eta| < 2.7$, respectively.

---

[1] Throughout this note, Z/γ^* boson production is denoted simply as Z boson production.

[2] ATLAS uses a right-handed coordinate system with its origin at the nominal interaction point (IP) in the centre of the detector and the z-axis along the beam pipe. The x-axis points from the IP to the centre of the LHC ring, and the y-axis points upward. Cylindrical coordinates (r, ϕ) are used in the transverse plane, ϕ being the azimuthal angle around the beam pipe. The pseudorapidity is defined in terms of the polar angle θ as $\eta = -\ln\tan(\theta/2)$.

A two-level trigger system is used to select events. The first-level trigger is implemented in hardware and uses a subset of the detector information. This is followed by the software-based High-Level Trigger (HLT) system, which can run offline reconstruction and calibration software, reducing the event rate to less than 1 kHz.

3 Cross-section methodology and theoretical predictions

3.1 Methodology

The production cross section for the $W^\pm$ boson $\sigma_{W^\pm}^{\text{tot}}$ times the branching ratio for decays into a single lepton flavour $BR(W \to \ell\nu)$ can be expressed as:

$$\sigma_{W^\pm}^{\text{tot}} = \sigma_W \cdot BR(W \to \ell\nu) = \frac{N_W^{\text{sig}}}{A_W \cdot C_W \cdot \mathcal{L}} \tag{1}$$

and similarly for σ_Z^{tot}, introducing N_Z^{sig}, $BR(Z \to \ell^+\ell^-)$, A_Z, and C_Z in place of the corresponding $W^\pm$ values. These factors are defined as follows:

- N_W^{sig} and N_Z^{sig} denote the numbers of background-subtracted data events ($N_{\text{observed}} - N_{\text{background}}$) passing the selection criteria of the analyses in the $W^\pm$ and Z boson channels.

- A_W and A_Z denote the acceptances for the $W^\pm$ and Z-boson decays under consideration, defined as the fraction of decays satisfying the geometric and kinematic requirements at the generator level (fiducial acceptance). These quantities can only be determined from Monte Carlo simulations and are defined before the decay leptons emit photons via final state radiation (Born-level FSR), unless otherwise stated.

- C_W and C_Z denote the ratios between the total number of generated events which pass the final selection requirements after reconstruction and the total number of generated events within the fiducial acceptance. These correction factors include the efficiencies for triggering, reconstructing, and identifying the $W^\pm$ and Z-boson decays falling within the acceptance, and an acceptance correction accounting for the slight difference between the fiducial phase space and the phase space selected in reconstruction. The denominators of the C ratios are conceptually equivalent to the numerators of the respective A ratios.

- $\mathcal{L}$ denotes the integrated luminosity of the data set used, which is the same for all analyses presented here.

The resulting cross sections, as defined by Eq. (1), define measured total inclusive cross sections and subsequent decay to a single lepton flavour. For the $W^\pm$ bosons, they are measured separately for W^+, W^- and $W^\pm$ production. The total cross sections are therefore denoted as $\sigma_{W^+}^{\text{tot}}$, $\sigma_{W^-}^{\text{tot}}$ and $\sigma_{W^\pm}^{\text{tot}}$. The corresponding Z boson cross section in the invariant mass range $66 < m_{\ell\ell} < 116$ GeV is referred to as σ_Z^{tot}.

The $W^\pm$ boson cross section in the fiducial region, $\sigma_{W^\pm}^{\text{fid}}$, is related to the total cross section via the formula:

$$\sigma_{W^\pm}^{\text{fid}} = \sigma_{W^\pm}^{\text{tot}} \cdot A_W = \frac{N_W^{\text{sig}}}{C_W \cdot \mathcal{L}} \tag{2}$$

and similarly for σ_Z^{fid}.

For the $W^\pm$ boson production cross section the fiducial phase space is defined by:

- $p_T^\ell > 25$ GeV
- $p_T^\nu > 25$ GeV
- $|\eta_\ell| < 2.5$
- $m_T > 50$ GeV

where p_T^ℓ is the lepton transverse momentum, η_ℓ is the lepton pseudorapidity, p_T^ν is the neutrino transverse momentum, and m_T is the transverse mass defined as

$$m_T = \sqrt{2p_T^\ell \, p_T^\nu \left[1 - \cos\left(\phi_\ell - \phi_\nu\right)\right]} \tag{3}$$

with ϕ_ℓ the azimuthal angle of the charged lepton, and ϕ_ν the azimuthal angle of the neutrino.

Similarly, the fiducial Z boson production cross section is measured in the fiducial phase space defined by:

- $p_T^\ell > 25$ GeV
- $|\eta_\ell| < 2.5$
- $66 < m_{\ell\ell} < 116$ GeV

where $m_{\ell\ell}$ is the dilepton invariant mass.

By definition, the acceptance correction factors A_W and A_Z are not included in the measurement of the fiducial cross section. As a result, these cross sections are not affected by significant theoretical uncertainties. Future improvements on the predictions of A_W or A_Z can be used to extract improved total cross-section measurements.

3.2 Theoretical predictions

The geometrical acceptances A_W and A_Z are calculated using Fewz3.1 [3–6] with the NNLO PDFs CT10NNLO [7]. The central values of the acceptances are provided in Table 1. The statistical uncertainties resulting from these evaluations are negligible.

The systematic uncertainties on the acceptance are dominated by the limited knowledge of the proton PDFs. The systematic uncertainties are derived from the following sources:

- PDF: These uncertainties are evaluated with four different NNLO PDFs: CT10NNLO, NNPDF3.0 [8], MMHT14NNLO68CL [9], and ABM12LHC [10]. The PDF uncertainty of the CT10NNLO PDF set was rescaled from 90% CL to 68% CL to match the other sets. The quadrature sum of the CT10NNLO eigenvectors uncertainties and the envelope of predictions from various PDFs set is taken as conservative estimate of the PDF uncertainties. The acceptance results determined with these alternate PDFs are presented in Table 1.

PDF	A_{W^+}	A_{W^-}	$A_{W^\pm}$	A_Z
CT10NNLO	$0.396^{+0.003}_{-0.003}$	$0.399^{+0.003}_{-0.004}$	$0.397^{+0.003}_{-0.003}$	$0.399^{+0.004}_{-0.005}$
NNPDF3.0	0.396	0.404	0.399	0.398
MMHT14NNLO	0.394	0.406	0.399	0.398
ABM12LHC	0.395	0.408	0.401	0.402

Table 1: Summary of geometrical acceptance values A_W and A_Z for $W \to \ell\nu$ and $Z \to \ell^+\ell^-$ using various PDF sets. The uncertainty in the top row is the CT10NNLO PDF set uncertainty. All other entries are the central value for the corresponding PDF set.

PDF	$\sigma^{\mathrm{fid}}_{W^+}$ [pb]	$\sigma^{\mathrm{fid}}_{W^-}$ [pb]	$\sigma^{\mathrm{fid}}_{W^\pm}$ [pb]	$\sigma^{\mathrm{fid}}_{Z}$ [pb]	$\sigma^{\mathrm{fid}}_{W^+}/\sigma^{\mathrm{fid}}_{W^-}$	$\sigma^{\mathrm{fid}}_{W^\pm}/\sigma^{\mathrm{fid}}_{Z}$
CT10NNLO	4660^{+110}_{-140}	3450^{+90}_{-110}	8110^{+190}_{-250}	769^{+20}_{-25}	$1.353^{+0.011}_{-0.012}$	$10.54^{+0.10}_{-0.12}$
NNPDF3.0	4500 ± 100	3400 ± 80	7890 ± 180	740 ± 16	1.324 ± 0.007	10.67 ± 0.06
MMHT14NNLO	4570^{+80}_{-60}	3500^{+60}_{-50}	8070^{+130}_{-110}	761^{+15}_{-13}	$1.307^{+0.010}_{-0.006}$	$10.61^{+0.10}_{-0.14}$
ABM12LHC	4650 ± 60	3510 ± 50	8150 ± 100	769 ± 10	1.326 ± 0.004	10.594 ± 0.035

Table 2: Summary of the fiducial $\sigma^{\mathrm{fid}}_{W^\pm}$ and $\sigma^{\mathrm{fid}}_{Z}$ predictions for $W \to \ell\nu$ and $Z \to \ell^+\ell^-$, and their ratios using various PDFs. The fiducial region is defined in Section 3.1. The uncertainties correspond to the PDF uncertainty.

- QCD scale: The scale uncertainies are defined by the envelope of variations in which the renormalisation (μ_R) and factorisation (μ_F) scales are changed by factors of two subject to the constraint $0.5 \leq \mu_R/\mu_F \leq 2$, which excludes variations in opposite directions. These uncertainies are symmetrised.

- α_S: The uncertainties due to α_S were estimated following the prescription given with the CT10NNLO PDF [7], varying α_S by ±0.001 to correspond to 68% CL. This source was found to be subdominant due to cancellation in the numerator and the denominatior of $A_{W,Z}$.

- Comparison of Fewz results with Powheg +Pythia 8 [11–14]: The difference between fixed-order predictions and Monte Carlo simulations was taken as an additional uncertainty.

- Parton showers and hadronisation description: These are taken from a previous publication of the $W^\pm$ and Z boson inclusive cross section [15] at 7 TeV.

These components, when added in quadrature, give the systematic uncertainties on the acceptance values for $W^\pm$ and Z boson production. The uncertainties were symmetrised by taking the larger of the upper and lower values for each component. The largest single source of uncertainty is the intrinsic PDF uncertainty. The total uncertainties on the acceptance correction factors are given in Tables 9 and 10.

Theoretical predictions of the fiducial and total cross sections are computed for comparison to the measured cross sections using Fewz 3.1, thereby providing full NLO EW and NNLO QCD calculations. The NLO EW corrections were calculated with Fewz 3.1 for Z bosons and with the Monte Carlo programme Sanc [16, 17] for $W^\pm$ bosons. The calculation was done in the G_μ EW scheme [18]. The cross sections were calculated for vector boson decays into leptons at Born level, to match the definition of the measured cross sections in the data. Thus, from complete NLO EW corrections the following components were included: virtual QED and weak corrections, real initial state radiation (ISR) and interference between ISR and real final state radiation (FSR) [19]. QED FSR effects as simulated in Photos [20] were used to correct the data. For the Z boson production, all the predictions are derived including the $66 < m_{\ell\ell} < 116\,\mathrm{GeV}$ requirement. The central values of the fiducial and total cross sections are provided in Tables 2 and 3, respectively. The statistical uncertainties resulting from these evaluations are negligible.

PDF	$\sigma_{W^+}^{\mathrm{tot}}$ [pb]	$\sigma_{W^-}^{\mathrm{tot}}$ [pb]	$\sigma_{W^\pm}^{\mathrm{tot}}$ [pb]	σ_Z^{tot} [pb]
CT10NNLO	11770^{+270}_{-310}	8640^{+210}_{-240}	20400^{+500}_{-500}	1930^{+40}_{-50}
NNPDF3.0	11360 ± 260	8410 ± 200	19800 ± 500	1860 ± 40
MMHT14NNLO	11610^{+200}_{-170}	8620^{+140}_{-130}	20230^{+330}_{-290}	1909^{+31}_{-27}
ABM12LHC	11760 ± 150	8580 ± 100	20340 ± 250	1914 ± 23

Table 3: Summary of the total $\sigma_{W^\pm}^{\mathrm{tot}}$ and σ_Z^{tot} predictions for $W \to \ell\nu$ and $Z \to \ell^+\ell^-$ using various PDFs. The uncertainties correspond to the PDF uncertainty.

Similarly to the acceptance factors $A_{W^\pm,Z}$, the systematic uncertainties on the predictions are dominated by the limited knowledge of the proton PDFs. Other major sources of systematic uncertainty on the predictions come from scale uncertainties and the uncertainty on α_S as described above. Additional sources of uncertainties come from:

- Knowledge of the beam energy: a systematic uncertainty of 1% has been assumed due to the uncertainty in the beam energy [21].

- EW corrections: these contribute of the order of 0.5% to the prediction uncertainty.

- Intrinsic theory uncertainties: these uncertainties are related to the limitations of NNLO calculations estimated by varying internal parameters related to the subtraction scheme and comparing to different codes. These are small for the total cross sections, and therefore were neglected. In the case of the fiducial cross sections, they are expected to contribute less than 1% to the prediction uncertainty.

The predictions for the fiducial cross sections using the CT10NNLO PDF set are:

- $\sigma_{W^+}^{\mathrm{fid}} = [4660^{+110}_{-140}(\mathrm{PDF}) \pm 70(\mathrm{scale}) \pm 85(\mathrm{other})]$ pb;

- $\sigma_{W^-}^{\mathrm{fid}} = [3450^{+90}_{-110}(\mathrm{PDF}) \pm 50(\mathrm{scale}) \pm 60(\mathrm{other})]$ pb;

- $\sigma_{W^\pm}^{\mathrm{fid}} = [8110^{+190}_{-250}(\mathrm{PDF}) \pm 120(\mathrm{scale}) \pm 145(\mathrm{other})]$ pb;

- $\sigma_Z^{\mathrm{fid}} = [769^{+20}_{-25}(\mathrm{PDF}) \pm 10(\mathrm{scale}) \pm 15(\mathrm{other})]$ pb.

while the predictions for the total cross sections are:

- $\sigma_{W^+}^{\mathrm{tot}} = [11770^{+270}_{-310}(\mathrm{PDF}) \pm 175(\mathrm{scale}) \pm 175(\mathrm{other})]$ pb;

- $\sigma_{W^-}^{\mathrm{tot}} = [8640^{+210}_{-240}(\mathrm{PDF}) \pm 130(\mathrm{scale}) \pm 130(\mathrm{other})]$ pb;

- $\sigma_{W^\pm}^{\mathrm{tot}} = [20400^{+500}_{-500}(\mathrm{PDF}) \pm 300(\mathrm{scale}) \pm 300(\mathrm{other})]$ pb;

- $\sigma_Z^{\mathrm{tot}} = [1930^{+40}_{-50}(\mathrm{PDF}) \pm 30(\mathrm{scale}) \pm 30(\mathrm{other})]$ pb

The first uncertainty corresponds to the variations of the CT10NNLO PDF set, the second to the variations of the scale, and the third to an estimate of all remaining systematic uncertainties described in this section, added in quadrature.

4 Dataset and simulated samples

The data were collected by the ATLAS detector during the period of June 13 to July 16, 2015. During this period, the LHC circulated 6.5 TeV proton beams with 50 ns bunch spacing. The peak delivered instantaneous luminosity was $L = 1.7 \times 10^{33}$ cm^{-1} s^{-1}, and the mean number of additional pp interactions per bunch crossing (pileup events) in the dataset was $\langle \mu \rangle = 19$.

The dataset is screened for problems with subdetector systems or operational inefficiencies, and the data passing these basic data-quality requirements correspond to a total integrated luminosity of 85 pb^{-1}. The uncertainty on the integrated luminosity is ±9%. It is derived, following a methodology similar to that detailed in Ref. [22], from a preliminary calibration of the luminosity scale using a pair of x-y beam separation scans performed in June 2015.

The data are compared to Monte Carlo simulations. Nearly all of the expected distributions were generated with the Powheg-Box v2 Monte Carlo program [11–13], specifically the codes for single boson production [23], interfaced with the Pythia v.8.186 parton shower program [14]. The programs used the CT10 PDF set [24] and the AZNLO CTEQL1 tune for Powheg +Pythia v.8 [25]. The EvtGen v.1.2.0 program [26] was used for properties of the bottom and charm hadron decays, and Photos++ version 3.52 was used for QED emissions from electroweak vertices and charged leptons.

Samples of top quark pairs production were generated with the Powheg-Box v2 generator and Pythia v.6.428 [27] (Perugia 2012 tune). The samples are normalised to the cross section calculated at NNLO + NNLL (next-to-next-to-leading-log) with the Top++2.0 program [28].

Diboson processes with four charged leptons, three charged leptons and one neutrino, or two charged leptons and two neutrinos were simulated using the Sherpa v2.1.1 generator [29]. The matrix elements contain the doubly-resonant WW, WZ and ZZ processes, and all other diagrams with four electroweak vertices. The 4ℓ and $2\ell + 2\nu$ processes were calculated at NLO for up to one additional parton; final states with two and three additional partons were calculated at LO. The $3\ell + 1\nu$ process was calculated at NLO and up to three partons at LO using the Comix [30] and OpenLoops [31] matrix element generators and merged with the Sherpa parton shower [32] using the ME+PS@NLO prescription [33]. The CT10 PDF set was used in conjunction with dedicated parton shower tuning.

Multijet events were simulated using Pythia v.8.186, and dedicated samples containing $b\bar{b}$ and $c\bar{c}$ quark final states were simulated using Pythia v.8.186 and the EvtGen v.1.2.0 program [26] in order to include the correct properties of the bottom and charm hadron decays.

To simulate the effects of additional proton-proton collisions in the same and nearby bunch crossings, additional events were generated using the soft QCD processes of Pythia v.8.186 using tune A2 [34] and the MSTW2008LO PDF. The Monte Carlo samples were reweighted so that the $\langle \mu \rangle$ distribution matched the observed distribution in the data. All of the samples were processed with the Geant4-based simulation [35] of the ATLAS detector [36].

An overview of all signal and background processes considered and of the generators used for the simulation is given in Table 4. Total production cross sections, including higher order QCD corrections and their respective uncertainties, are listed in Table 4 for the electroweak ($W^\pm$, Z and diboson) and $t\bar{t}$ processes.

For the comparison to data, all the Monte Carlo simulations, except the dijet samples, are normalised to the results of higher order QCD calculations listed in Table 4. For the multijet background, no reliable

Physics process	Generator	σ ($\cdot$ BR [pb])	Order	Reference
$W \to \ell\nu$ ($\ell = e, \mu, \tau$)	POWHEG +PYTHIA 8	$20400 \pm 5\%$	NNLO	[3–6]
$W^+ \to \ell^+\nu$		$11770 \pm 5\%$	NNLO	[3–6]
$W^- \to \ell^-\bar{\nu}$		$8640 \pm 5\%$	NNLO	[3–6]
$Z \to \ell^+\ell^-$ ($66 < m_{\ell\ell} < 116$ GeV)	POWHEG +PYTHIA 8	$1930 \pm 5\%$	NNLO	[3–6]
$t\bar{t}$ ($m_t = 172.5$ GeV)	POWHEG +PYTHIA 6	$830 \pm 6\%$	NNLO+NNLL	[28]
Dibosons	SHERPA	$99 \pm 6\%$	NLO	[29]
Dijet (e channel, $\hat{p}_T > 21$ GeV)	PYTHIA 8	180×10^3	LO	[14]
$b\bar{b}$ (μ channel, $\hat{p}_T > 15$ GeV)	PYTHIA 8	188	LO	[14]
$c\bar{c}$ (μ channel, $\hat{p}_T > 15$ GeV)	PYTHIA 8	58	LO	[14]

Table 4: Signal and background Monte Carlo samples from the generators used in the simulation. Each sample is normalised to the production cross section multiplied by the relevant branching ratios (BR), as shown in the third column. For the electroweak ($W^\pm$ and Z boson) and top-quark production, contributions from higher order QCD corrections are included following the references given in the last column. The diboson samples include WW, WZ and ZZ on-shell and off-shell production. The inclusive jet and heavy quark cross sections are calculated only at LO. These samples were generated with requirements on the transverse momentum of the partons involved in the hard-scattering process, $\hat{p}_T$.

prediction can be obtained from a leading order Monte Carlo simulation. For the final inclusive cross-section measurements, data-driven methods are used to determine the residual contributions of the multijet background to the $W^\pm$ boson samples, as discussed in Section 6.

5 Event selection

Electron and muon candidate events are selected using triggers that require at least one electron or muon with transverse momentum thresholds of $p_T > 24$ GeV and 20 GeV, respectively, with loose isolation requirements. To recover possible efficiency loss at high momenta, additional electron and muon triggers that do not make any isolation requirements are included with thresholds of $p_T > 60$ GeV and 50 GeV, respectively.

Candidate events are required to have a primary vertex, defined as the vertex with the highest sum of track p_T^2, with at least two associated tracks.

Electron candidates are reconstructed from an isolated electromagnetic calorimeter energy deposit matched to an inner detector track and are required to have $p_T > 25$ GeV and to pass a medium likelihood-based identification requirement [37], within the fiducial region of pseudorapidity $|\eta| < 2.47$. Candidates within the transition region between the barrel and endcap electromagnetic calorimeters, $1.37 < |\eta| < 1.52$, are removed. The likelihood includes measurements of calorimeter shower shapes and measurements of track properties from the inner detector. The electrons must also satisfy a p_T-dependent cone-based isolation requirement. The isolation requirement is based on both calorimeter and tracker information, and it is tuned so that the electron isolation efficiency is at least 90% for all $p_T > 25$ GeV.

Muons are reconstructed in the region $|\eta| < 2.4$ from muon spectrometer tracks and matching inner detector tracks. All muons must have $p_T > 25$ GeV and must pass the "medium" identification requirements, based on requirements on the number of hits in the different inner detector and muon spectrometer subsystems, and the q/p significance [38]. They must also satisfy the same p_T-dependent cone-based isolation requirements, tuned so that the muon isolation efficiency is at least 90% for $p_T > 25$ GeV.

Jets are reconstructed from calorimeter clusters using the anti-k_T algorithm [39] with radius parameter $R = 0.4$ using topological clusters in the calorimeter as input objects. All jets must have $p_T > 20$ GeV and pseudorapidity requirement $|\eta| < 4.5$. Jets are calibrated as described in Ref. [40]. In order to reduce the effects of pileup contributions, a significant fraction of tracks in each jet are required to have origins compatible with the primary vertex, as defined in the jet vertex tagger [41], and the expected average contribution from pileup clusters is subtracted according to the jet area.

The missing transverse momentum vector (E_T^{miss}) is defined as the negative of the global vector sum of all identified physics objects (electrons, muons, jets) as well as specific "soft terms" accounting for unclassified soft tracks and calorimeter clusters. In this way, the missing transverse momentum is adjusted for the best calibration of the jets and the other identified physics objects above.

The $W^\pm$ boson signature event selection requires exactly one identified electron or muon. If a second lepton passing the same quality and kinematic requirements is present in the event, the event is rejected. The magnitude of the calibrated missing transverse momentum is required to be $E_T^{\text{miss}} > 25$ GeV, and the transverse mass[3] is required to satisfy $m_T > 50$ GeV. After the full $W \rightarrow \ell\nu$ selection a total of 463063 candidates (256923 e^+ and 206140 e^-) pass all requirements in the electron channel, and 487090 candidates (272841 μ^+ and 214249 μ^-) pass the requirements in the muon channel.

Events containing a Z boson candidate are selected by requiring exactly two selected leptons of the same flavor that are oppositely charged. The invariant mass of the dilepton pair has to satisfy $66 < m_{\ell\ell} < 116$ GeV. A total of 34955 candidates pass all requirements in the electron channel and 44899 candidates in the muon channel.

6 Background contributions to $W^\pm$ and Z boson selections

Contributions from the electroweak (single boson and diboson) and top-quark components of the background are obtained from the corresponding Monte Carlo samples described in Section 4. Table 5 shows the expected contributions of individual background processes in the W and Z channel. All other sources of electroweak background are expected to be negligible.

In the inclusive $W^\pm$ boson analysis, the multijet component of the background is estimated from the data. In the inclusive Z boson analysis, studies of the data invariant mass sidebands show that the multijet component is less than 0.1% of the data sample.

In the $W^\pm$ boson analysis the multijet background is estimated using the transverse mass (m_T) distribution in the data, because the low m_T tail outside the signal region is largely populated by multijet events. Events are selected by applying all of the $W^\pm$ boson selection, except the m_T threshold at 50 GeV. The expected number of multijet events is then extracted using a binned maximum likelihood template fit on the entire m_T spectrum, separately for events selected with positively charged leptons and negatively charged leptons. The signal and multijet background yields are free parameters in the fits. The other background components are normalised to their expectation, based on the estimated cross section and integrated luminosity. Systematic uncertainties on these expected yields are applied through multiplicative scale factors on the yields, and Gaussian constraint terms for these scale factors are included in the likelihood fit. The fit templates for the $W^\pm$ signal and for the dominant electroweak and top-quark backgrounds

---

[3] The transverse mass is defined by Eq. 3, where p_T^ν and ϕ_ν are estimated from the measured E_T^{miss} vector.

	Expected fraction in each channel			
	$W \to e\nu$	$W \to \mu\nu$	$Z \to e^+e^-$	$Z \to \mu^+\mu^-$
$W \to \tau\nu$	1.8	2.0	–	–
$Z \to \tau^-\tau^-$	0.2	0.2	<0.1	<0.1
Diboson	–	–	0.1	0.1
$t\bar{t}$	1.2	1.1	0.5	0.5
$W \to e\nu$	95.6	–	<0.1	–
$W \to \mu\nu$	–	92.0	–	<0.1
$Z \to e^+e^-$	1.2	–	99.4	–
$Z \to \mu^+\mu^-$	–	4.7	–	99.4

Table 5: Electroweak and top-quark background contributions estimated from simulation for the inclusive channels. Expectations are expressed as a percentage of the total number of simulated events passing the signal selection in each channel. Sources of background that were found to be negligible in comparison with the others are indicated by a dash. The total number of events and the associated uncertainties are given in Table 6.
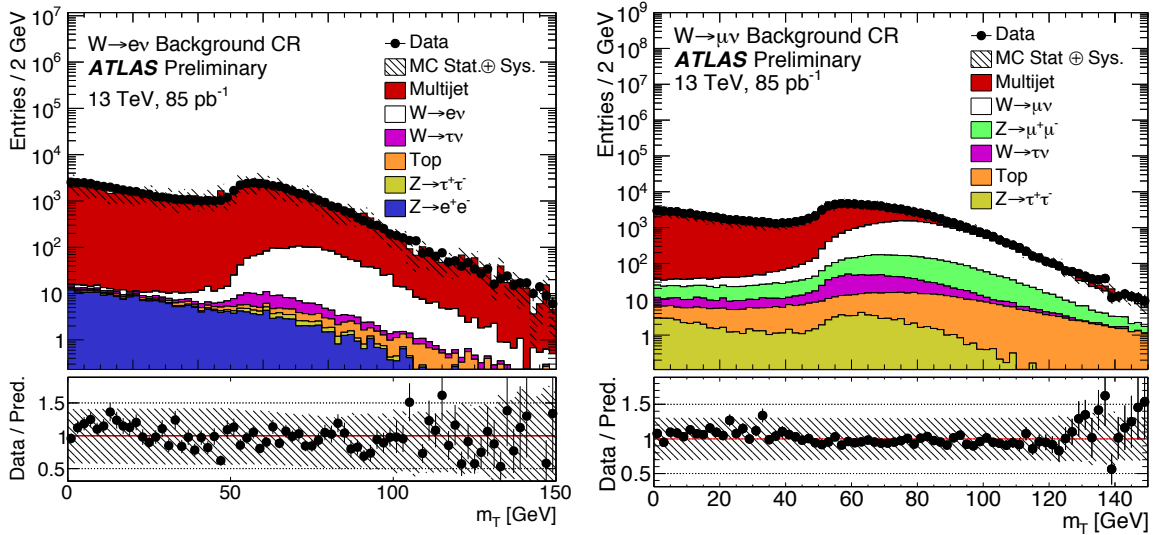
Figure 1: The $W^\pm$ boson transverse mass spectrum reconstructed in the electron (left) and muon (right) channel, for events passing the control region selection described in the text.

are taken from Monte Carlo simulation, whereas the shape of the multijet background is determined from data, as described in the following for the electron and the muon channel.

$W \to e\nu$ **channel:** The multijet background expectation in the $W \to e\nu$ channel includes heavy-quark decays, converted photons, and hadrons mimicking the detector signature of electrons. A template derived from data with a modified electron selection (control region) is used to fit the $W^\pm$ boson transverse mass distribution. The background template is obtained by using the $W^\pm$ boson selection, but reversing some of the requirements in the medium electron identification, and relaxing the isolation requirement. Some events from signal, electroweak, and top-quark processes pass the control region selection. This contamination is estimated to be about 3% and is subtracted from the data. Figure 1 (left) shows the m_T distribution for the data and the signal and background Monte Carlo samples in the control region.

The systematic uncertainty on the fitted background yield is estimated by inverting the isolation require-

$\ell^\pm$	Observed candidates	Background (EW+top)	Background (Multijet)	Background-subtracted events N_W^{sig}
e^+	256923	10100 ± 600	$15200 \pm 300 \pm 6700$	$231600 \pm 500 \pm 6700$
e^-	206140	8900 ± 500	$15600 \pm 300 \pm 6900$	$181600 \pm 500 \pm 6900$
μ^+	272841	20420 ± 920	$12200 \pm 200 \pm 3500$	$240300 \pm 500 \pm 3600$
μ^-	214249	18210 ± 830	$11500 \pm 100 \pm 3100$	$184500 \pm 500 \pm 3200$

Table 6: Number of observed events in the $W \to \ell\nu$ channels, electroweak plus top-quark background (EW+top), and data-derived multijet background events, and background-subtracted data events. The first uncertainty is statistical. The second uncertainty represents the systematic uncertainties, as described in the text. The uncertainty considered for the EW+top backgrounds is the combination of the experimental uncertainties, the NNLO normalisation uncertainties, and the small statistical uncertainty from the Monte Carlo samples. The 9% uncertainty on the luminosity determination, applicable to the EW+top backgrounds, is not included in this table.

ment in the data control region and repeating the fit using this modified template. Based on this study, the systematic uncertainty on the multijet background is estimated to be approximately 40%.

The numbers of multijet events extracted in the signal region ($m_{\text{T}} > 50$ GeV) are $N_{\text{Multijet}}^{e^+} = 15200 \pm 300 \pm 6700$ events and $N_{\text{Multijet}}^{e^-} = 15600 \pm 300 \pm 6900$ events, where the uncertainty contributions are statistical and systematic, in that order.

$W \to \mu\nu$ **channel:** The main sources of multijet background for the $W \to \mu\nu$ channel are non-prompt muons from b and c hadron decays. This background is modelled from data using a template built in a background-enriched control region, where the full analysis selection is applied but the isolation requirement on the muons is inverted. Those requirements ensure that the control region is orthogonal to the signal region, and reduce the signal contribution in the control region. Figure 1 (right) shows the m_{T} distribution in the control region defined above. The contamination of the multijet-enriched control region by signal and non-multijet backgrounds is estimated to be 20%. Templates are derived from the data after subtracting this contamination according to its estimate from simulation.

The total systematic uncertainty includes the uncertainties on the yield of the other background components, a possible difference in the relative proportions of $b\bar{b}$ and $c\bar{c}$ between the signal region and the control region estimated with simulation, and shape differences between the nominal data template and templates with different background subtraction scenarios. The main source of systematic uncertainty ($\sim 20\%$) comes from the difference between the fit results obtained using the nominal data template and a template built from an alternative data control region where the isolation requirement is unchanged with respect to the signal selection but the muon candidates are required to have a large impact parameter significance.

The number of multijet events returned by the fit is then extracted in the signal region with $m_{\text{T}} > 50$ GeV. This results in an estimate of $N_{\text{Multijet}}^{\mu^+} = 12200 \pm 200 \pm 3500$ events and $N_{\text{Multijet}}^{\mu^-} = 11500 \pm 100 \pm 3100$ events, where the uncertainty contributions are statistical and systematic, in that order.

$\ell^\pm$	Observed candidates	Background (EW+top)	Background (Multijet)	Background-subtracted events N_Z^{sig}
$e^\pm$	34955	$229 \pm 1 \pm 24$	$< 0.1\%$	$34730 \pm 190 \pm 20$
$\mu^\pm$	44899	$296 \pm 2 \pm 31$	$< 0.1\%$	$44600 \pm 210 \pm 30$

Table 7: Number of observed events in the $Z \to \ell^+\ell^-$ channels, and estimates for the electroweak plus top-quark background (EW+top), the multijet background, and background-subtracted data events. The first uncertainty is statistical. The second uncertainty represents the systematic uncertainties, as described in the text. The 9% uncertainty on the luminosity determination, applicable to the EW+top backgrounds, is not included in this table.

7 $W^\pm$ and Z boson candidates

For the $W \to \ell\nu$ and $Z \to \ell^+\ell^-$ channels, the number of observed candidate events, the estimated backgrounds from the multijet and electroweak plus top-quark processes, and the background-subtracted signal yields are summarised in Tables 6 and 7, together with their statistical and systematic uncertainties. The systematic uncertainties on the backgrounds include contributions from experimental sources and from theoretical uncertainties on the predicted cross sections for $W^\pm$, Z (due to cross-contamination between channels) and top-quark production. The background-subtracted data result includes the statistical uncertainty and the total systematic uncertainty, obtained by summing in quadrature the EW+top uncertainties and the multijet statistical and systematic uncertainties. For the $Z \to \ell^+\ell^-$ channels, the multijet background is estimated to have less than a 0.1% contribution to the cross-section measurement and is therefore neglected. All results from Monte Carlo samples have negligible statistical uncertainties.

The luminosity determination uncertainty of $\pm 9\%$ is used in all channels but is only applicable to the electroweak and top-quark backgrounds as they are determined from Monte Carlo samples. The resulting correlation of the luminosity systematic uncertainty is fully taken into account in the calculation of the cross sections in Section 8.2.

Kinematic distributions are shown in Figs. 2-9 for the $W \to e\nu$ and $W \to \mu\nu$ channels, and in Figs. 10-16 for the $Z \to e^+e^-$ and $Z \to \mu^+\mu^-$ channels. The uncertainty bands shown in these distributions are described in Section 8.1 and are calculated from the following components:

- uncertainty due to the multijet background estimation method;

- lepton energy and momentum scale and resolution;

- lepton trigger efficiency;[4]

- lepton reconstruction and identification efficiency, including uncertainties on lepton isolation;

- jet energy scale and resolution;

- soft (unclustered) energy contributions in the E_T^{miss} reconstruction;

- uncertainties in background cross-section calculations for electroweak and top-quark production;

---

[4] Due to the limited data set available, the data over Monte Carlo correction factors for the muon trigger efficiency were evaluated in coarser bins than the one used in the kinematic plots. Therefore, the uncertainties are not expected to cover discrepancies observed on a smaller pseudorapidity range.
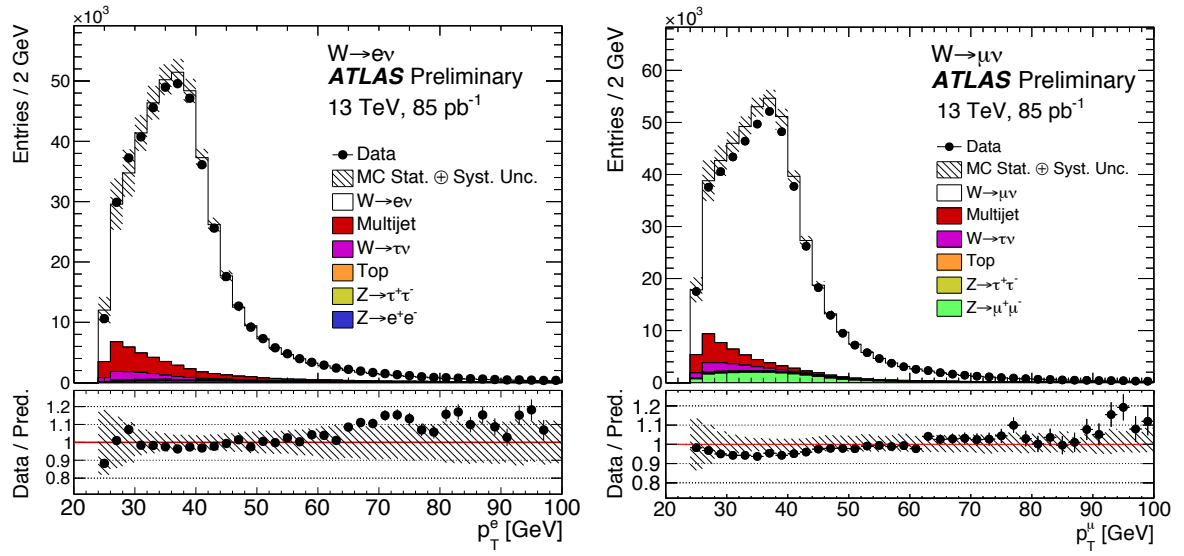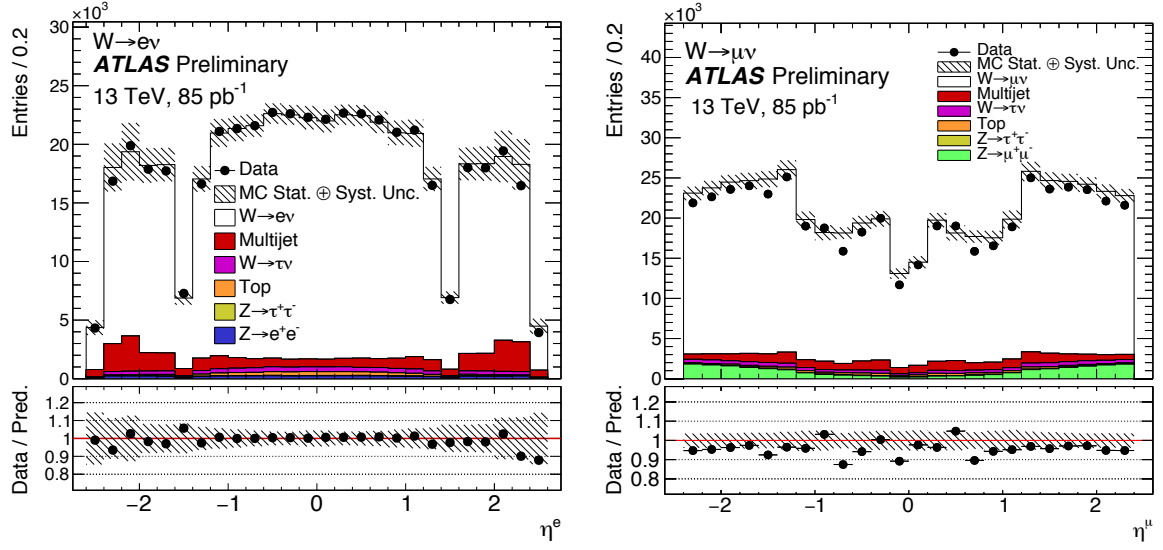
Figure 2: Lepton transverse momentum distribution from the $W \rightarrow e\nu$ selection (left) and the $W \rightarrow \mu\nu$ selection (right). The expected contributions from all backgrounds are estimated with Monte Carlo simulations, except for the multijet background which is estimated with a data-driven method. Systematic uncertainties for the signal and background distributions are combined in the shaded band, the statistical uncertainty is shown on the data points. The luminosity uncertainty is not included.

- statistical uncertainty due to limited Monte Carlo sample size.

These uncertainties are included in the histograms as a shaded band, but the 5% theoretical uncertainty on the $W^\pm$ and Z signal cross section and the luminosity uncertainty of $\pm 9\%$ are omitted from the band.

Figure 3: Lepton pseudorapidity distribution from the $W \to e\nu$ selection (left) and the $W \to \mu\nu$ selection (right). The expected contributions from all backgrounds are estimated with Monte Carlo simulations, except for the multijet background which is estimated with a data-driven method. Systematic uncertainties for the signal and background distributions are combined in the shaded band, the statistical uncertainty is shown on the data points. The luminosity uncertainty is not included.
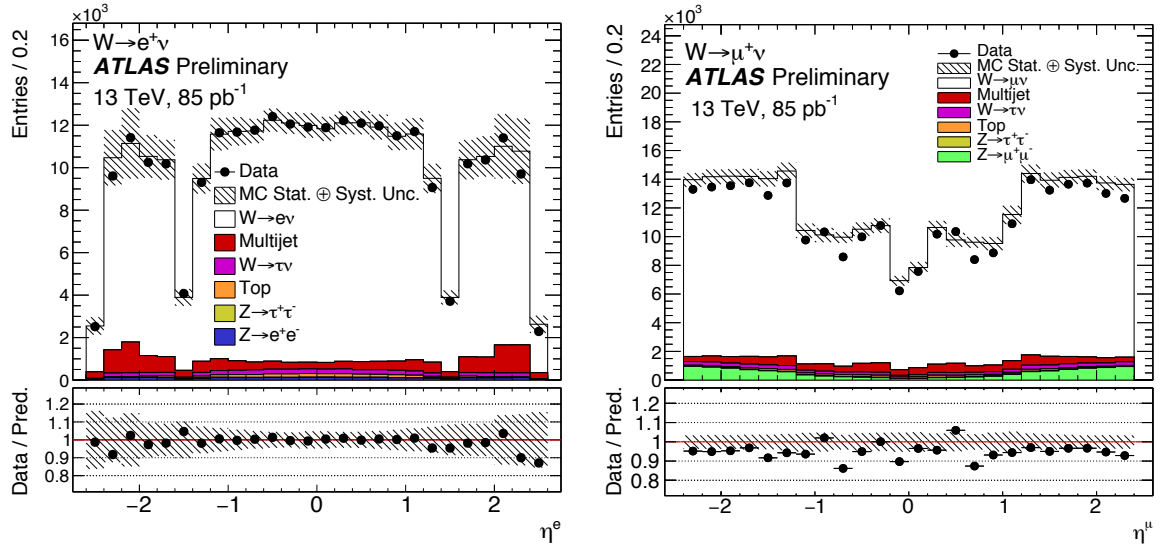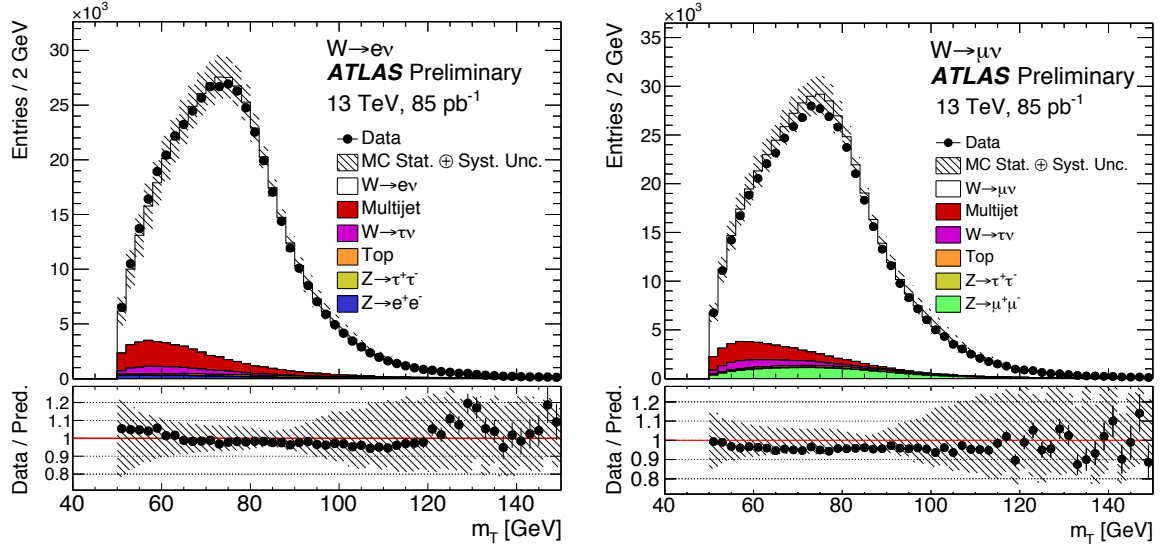

Figure 4: Lepton pseudorapidity distribution as described in Figure 3, but for positively charged leptons only.
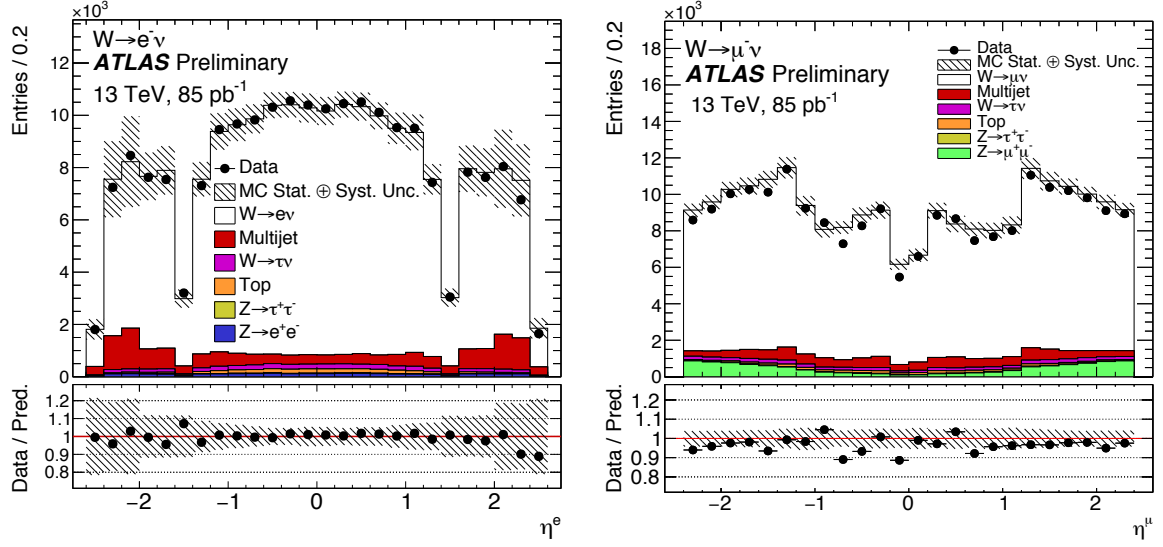
Figure 5: Lepton pseudorapidity distribution as described in Figure 3 but for negatively charged leptons only.
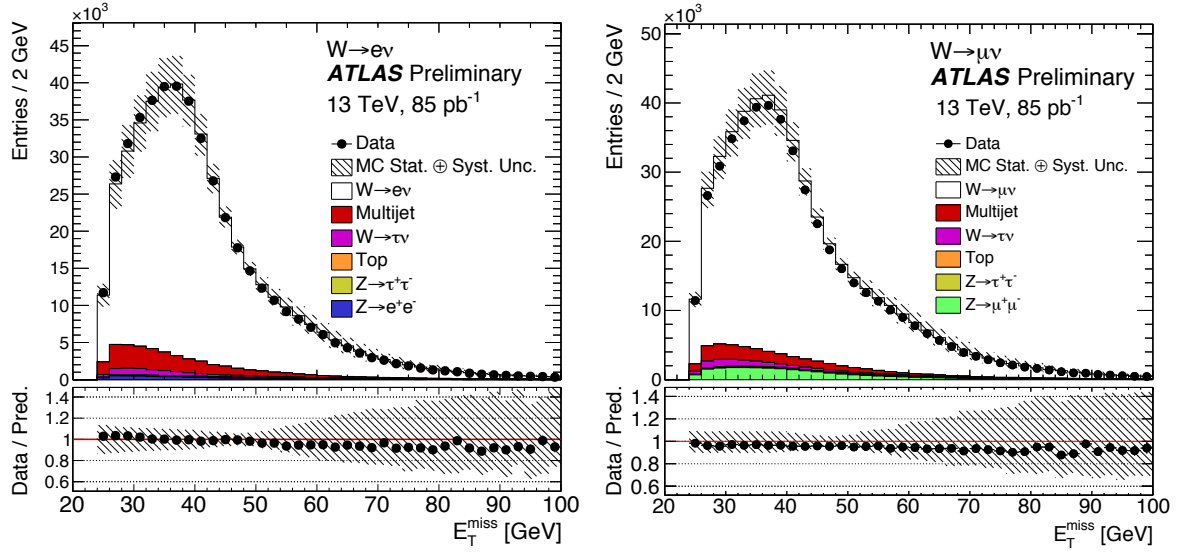
Figure 6: Missing transverse energy distribution from the $W \rightarrow e\nu$ selection (left) and the $W \rightarrow \mu\nu$ selection (right). The E_T^{miss} has been recalibrated using the best energy calibration for each of the identified physics objects. The expected contributions from all backgrounds are estimated with Monte Carlo simulations, except for the multijet background which is estimated with a data-driven method. Systematic uncertainties for the signal and background distributions are combined in the shaded band, the statistical uncertainty is shown on the data points. The luminosity uncertainty is not included.
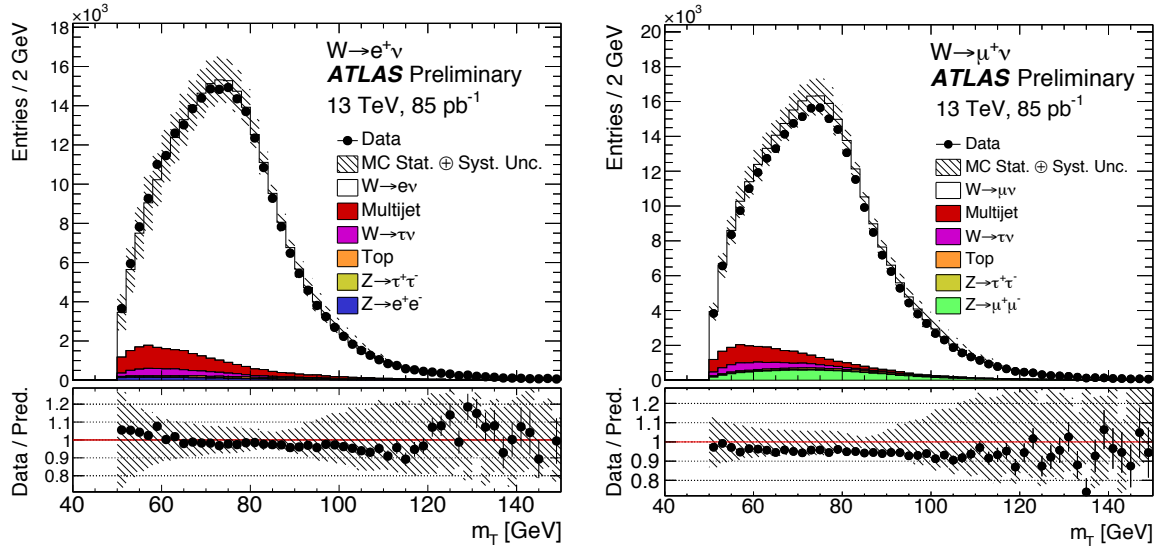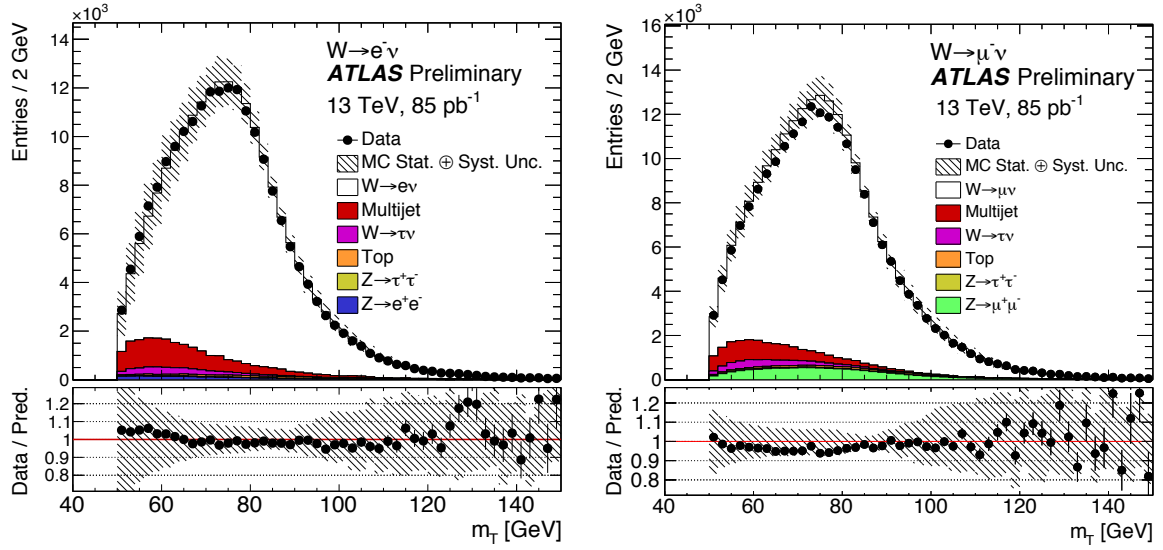
Figure 7: Transverse mass distribution, calculated from the lepton and the E_T^{miss} from the $W \to e\nu$ selection (left) and the $W \to \mu\nu$ selection (right). The expected contributions from all backgrounds are estimated with Monte Carlo simulations, except for the multijet background which is estimated with a data-driven method. Systematic uncertainties for the signal and background distributions are combined in the shaded band, the statistical uncertainty is shown on the data points. The luminosity uncertainty is not included.

Figure 8: Transverse mass distribution as described in Figure 7 but for positively charged leptons only.

Figure 9: Transverse mass distribution as described in Figure 7 but for negatively charged leptons only.
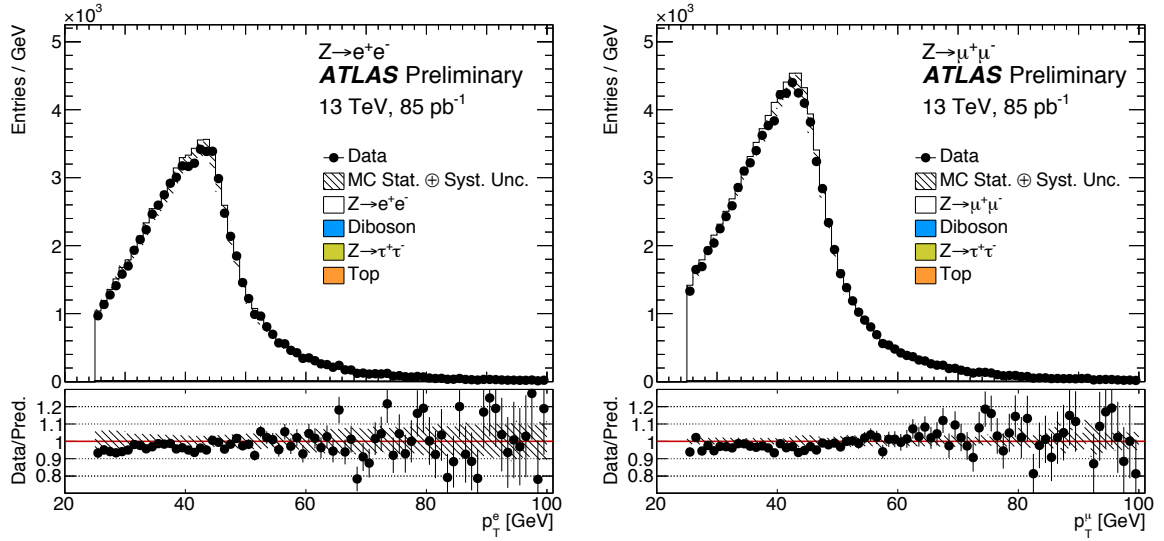

Figure 10: Lepton transverse momentum distributions from the $Z \rightarrow e^+e^-$ selection (left) and the $Z \rightarrow \mu^+\mu^-$ selection (right). The expected contributions from all backgrounds are estimated with Monte Carlo simulations. The background processes are heavily suppressed and not visible on the linear scale. Systematic uncertainties for the signal and background distributions are combined in the shaded band, the statistical uncertainty is shown on the data points. The luminosity uncertainty is not included. There are two lepton entries in the histogram for each candidate event.
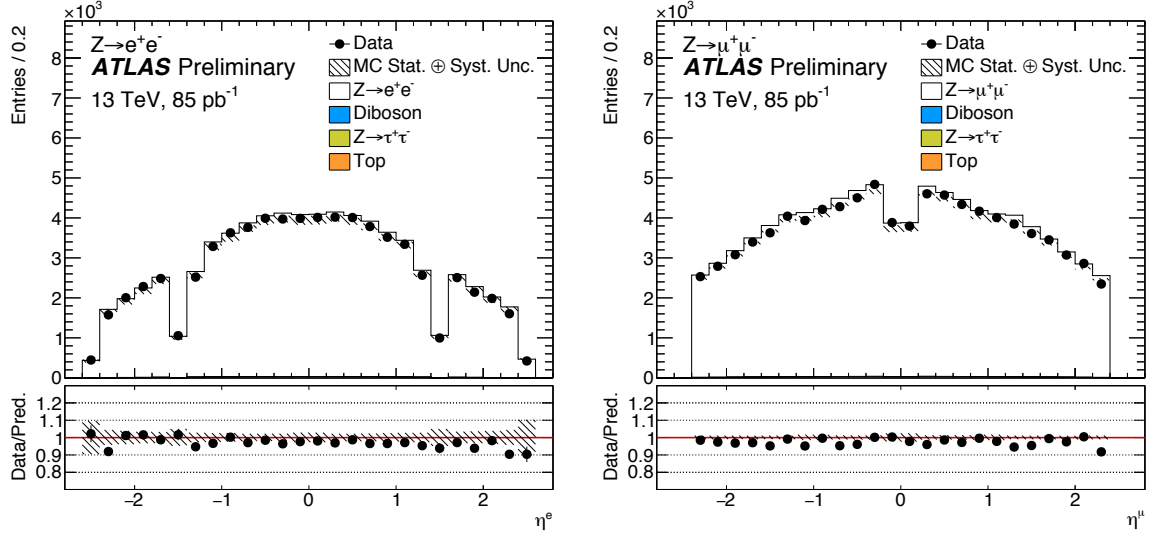
Figure 11: Lepton pseudorapidity distribution from the $Z \rightarrow e^+e^-$ selection (left) and the $Z \rightarrow \mu^+\mu^-$ selection (right). The expected contributions from all backgrounds are estimated with Monte Carlo simulations. The background processes are heavily suppressed and not visible on the linear scale. Systematic uncertainties for the signal and background distributions are combined in the shaded band, and the statistical uncertainty is shown on the data points. The luminosity uncertainty is not included. There are two lepton entries in the histogram for each candidate event.
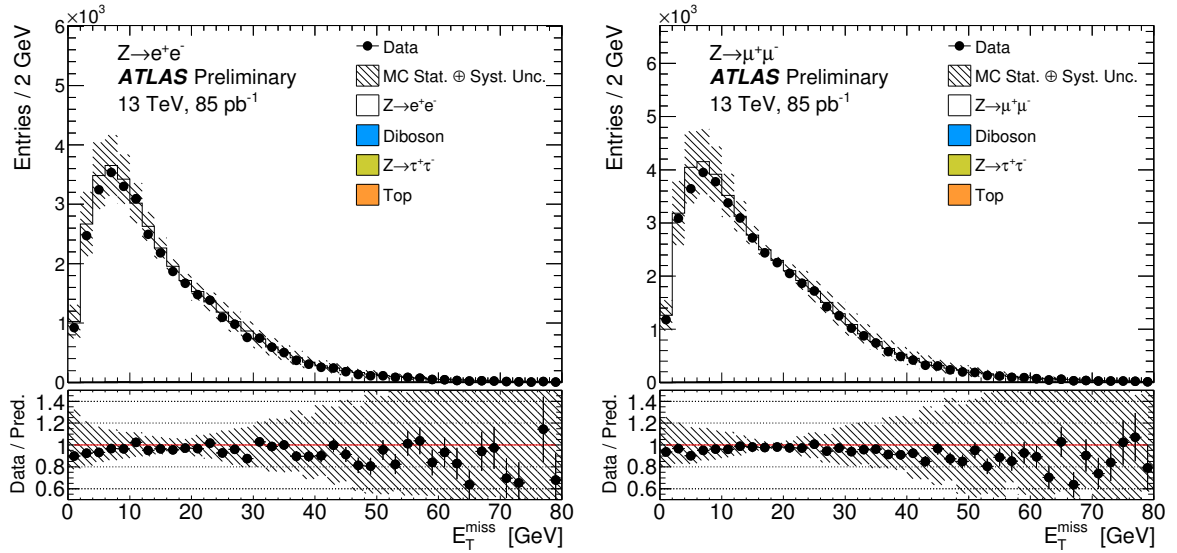

Figure 12: Missing transverse energy distribution from the $Z \rightarrow e^+e^-$ selection (left) and the $Z \rightarrow \mu^+\mu^-$ selection (right). The E_T^{miss} has been recalibrated using the best energy calibration for the physics objects. The expected contributions from all backgrounds are estimated with Monte Carlo simulations. The background processes are heavily suppressed and not visible on the linear scale. Systematic uncertainties for the signal and background distributions are combined in the shaded band, and the statistical uncertainty is shown on the data points. The luminosity uncertainty is not included.
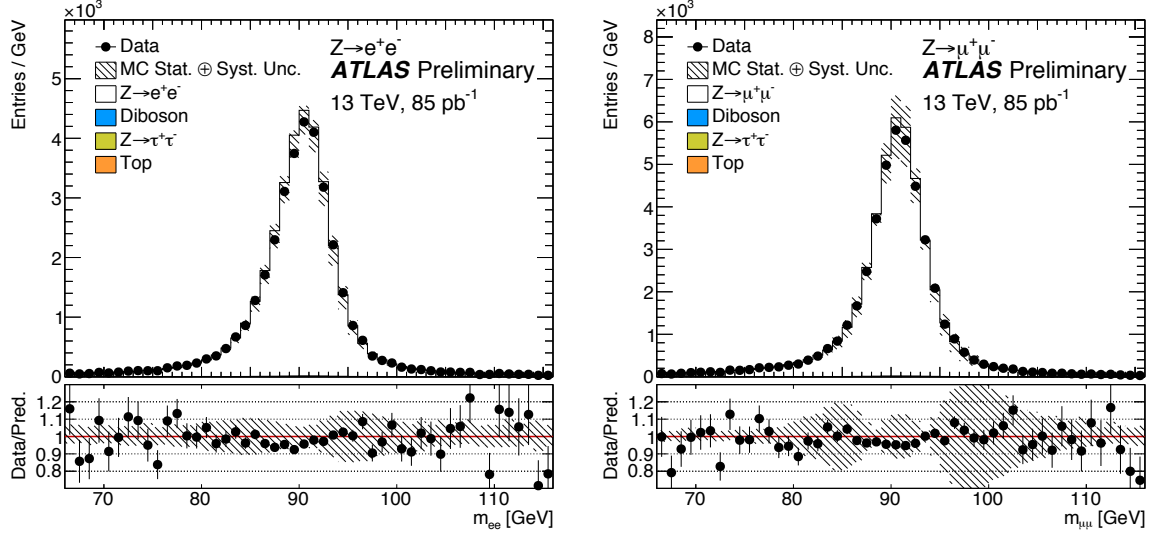
Figure 13: Dilepton mass distribution after the $Z \rightarrow e^+e^-$ selection (left) and the $Z \rightarrow \mu^+\mu^-$ selection (right). The expected contributions from all backgrounds are estimated with Monte Carlo simulations. The background processes are heavily suppressed and not visible on the linear scale. Systematic uncertainties for the signal and background distributions are combined in the shaded band, and the statistical uncertainty is shown on the data points. The luminosity uncertainty is not included.
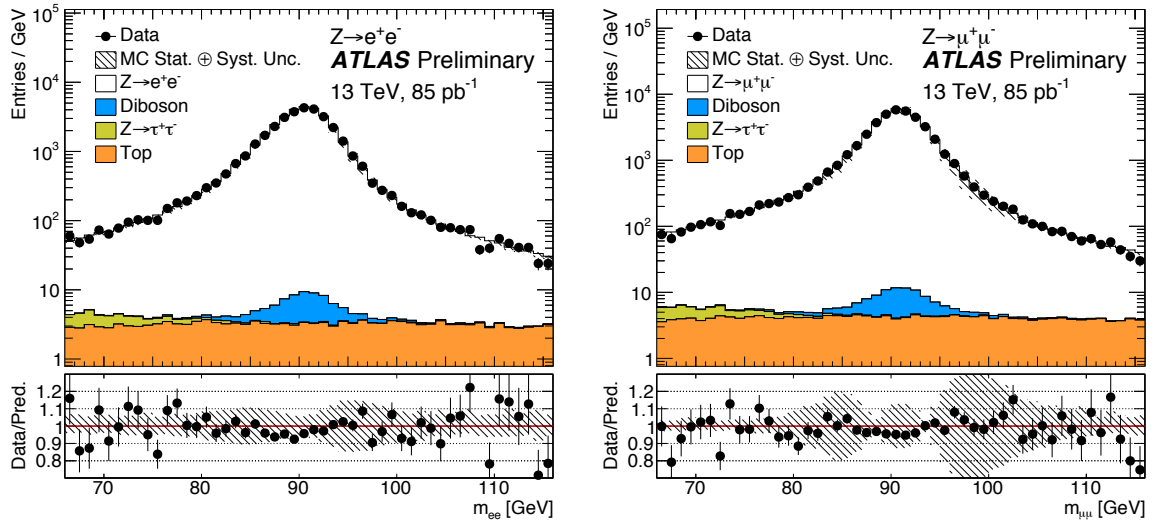

Figure 14: Dilepton mass distribution after the $Z \rightarrow e^+e^-$ selection (left) and the $Z \rightarrow \mu^+\mu^-$ selection (right). The expected contributions from all backgrounds are estimated with Monte Carlo simulations. Systematic uncertainties for the signal and background distributions are combined in the shaded band, and the statistical uncertainty is shown on the data points. The luminosity uncertainty is not included.

Figure 15: Z boson transverse momentum distribution after the $Z \rightarrow e^+e^-$ selection (left) and the $Z \rightarrow \mu^+\mu^-$ selection (right). The expected contributions from all backgrounds are estimated with Monte Carlo simulations. Systematic uncertainties for the signal and background distributions are combined in the shaded band, and the statistical uncertainty is shown on the data points. The luminosity uncertainty is not included.
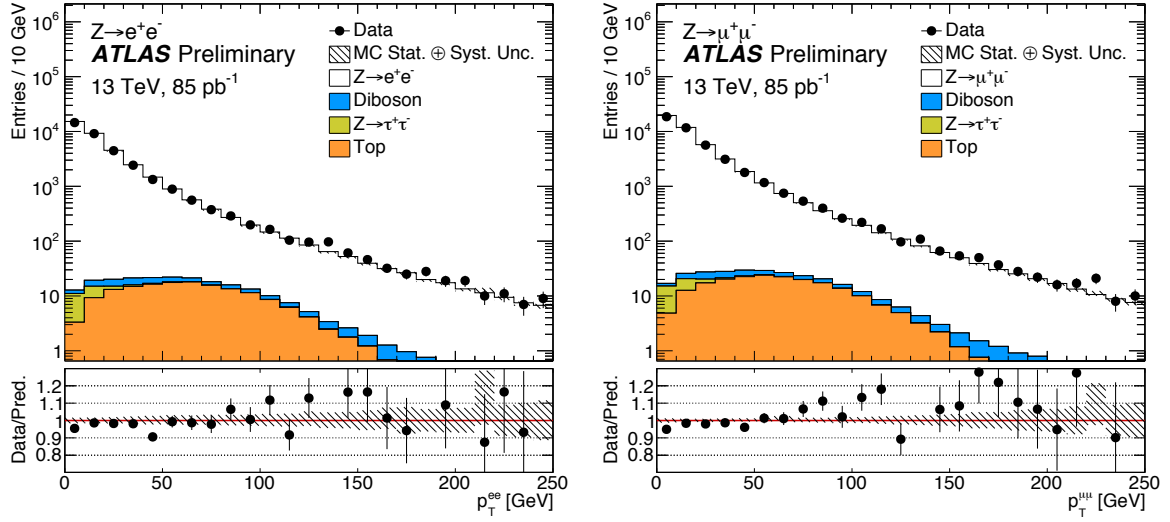

Figure 16: Z boson rapidity distribution after the $Z \rightarrow e^+e^-$ selection (left) and the $Z \rightarrow \mu^+\mu^-$ selection (right). The expected contributions from all backgrounds are estimated with Monte Carlo simulations. The background processes are heavily suppressed and not visible on the linear scale. Systematic uncertainties for the signal and background distributions are combined in the shaded band, and the statistical uncertainty is shown on the data points. The luminosity uncertainty is not included.
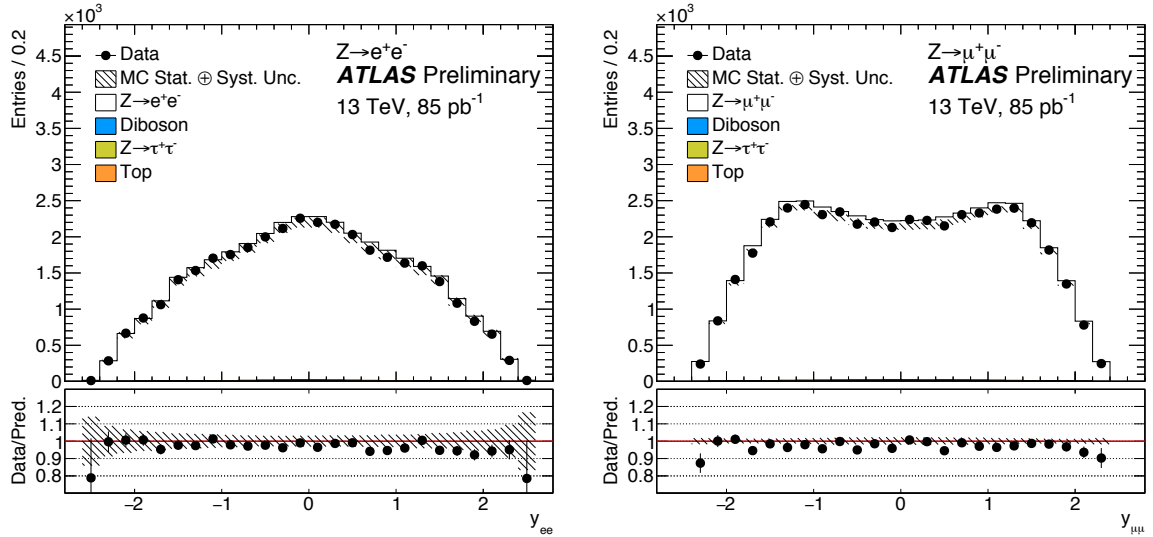
8 Cross-section measurements and results

8.1 Correction factors C_W and C_Z and their uncertainties

The central values of the correction factors C_W and C_Z are computed using a combination of simulation and corrections based on data. Several important components such as lepton reconstruction, identification, and trigger efficiencies feed into the evaluation of C_W and C_Z and their systematic uncertainties. These efficiencies have been measured with Monte Carlo samples and corrected by data-driven scale factors to take into account differences between data and simulation. The correction factors C_W and C_Z include the effects of detector efficiencies. The following decomposition is used to assess the uncertainties:

$$C_W = \epsilon_{\text{event}}^W \cdot \alpha_{\text{reco}}^W \cdot \epsilon_{\text{lep}}^W \cdot \epsilon_{\text{trig}}^W \tag{4}$$

$$C_Z = \epsilon_{\text{event}}^Z \cdot \alpha_{\text{reco}}^Z \cdot \left(\epsilon_{\text{lep}1}^Z \right) \cdot \left(\epsilon_{\text{lep}2}^Z \right) \cdot \left[1 - \left(1 - \epsilon_{\text{trig}1}^Z \right) \left(1 - \epsilon_{\text{trig}2}^Z \right) \right],$$

where the individual factors account for event selection efficiencies (ϵ_{event}), e.g. primary vertex requirements; the reconstruction corrrection factor α_{reco} (described below); lepton reconstruction, identification and isolation efficiencies (ϵ_{lep}); and the trigger efficiency for selected lepton candidates (ϵ_{trig}). The exact definitions of these factors for the electron and muon final states are given below.

The factor α_{reco} accounts for all differences observed between the efficiencies of applying the kinematic and geometrical selection at generator level and reconstruction level. It includes, for example, effects due to the detector resolution on the lepton transverse momenta/energies and on the missing transverse energy. This factor also includes basic reconstruction efficiencies. The choice mentioned above of calculating the acceptance factors $A_{W,Z}$ for leptons before they emit final-state radiation of photons also affects this correction factor in a significant way, in particular for electron final states. Finally, this factor includes migration and combinatorial effects and may therefore have values larger than unity.

The contributions to the systematic uncertainties on the C correction factors are described below and summarised in Table 8. The final values for $C_{W,Z}$ are presented in Tables 9 and 10.

Uncertainties specific to the electron channel are:

- **Trigger:** A dedicated data-driven analysis is performed to obtain the trigger scale factors and the corresponding uncertainty from the data. The trigger efficiency uncertainty affects the $W^\pm$ boson measurement more than the Z boson measurement since for Z boson events one of the two leptons is sufficient to trigger the event.

- **Identification and Reconstruction:** The efficiency in the simulation of the electron offline selection (reconstruction, application of the medium likelihood working point, and isolation) is corrected with data, and specific scale factors with associated statistical and systematic uncertainties are applied to simulation. The dominant uncertainty is associated with the electron identification. The impact on the Z boson measurement is twice as large as for the $W^\pm$ boson.

- **Energy Scale and Resolution:** The uncertainties on the electron energy calibration cause a small change of acceptance because of migration of events below and above the p_T threshold and across the $m_{\ell\ell}$ boundaries in the $Z \to \ell^+\ell^-$ channels. This yields a small uncertainty on the measurement.

Process $\delta C/C$ (%)	$Z \to \mu^+\mu^-$	$W^+ \to \mu^+\nu$	$W^- \to \mu^-\bar{\nu}$	$Z \to e^+e^-$	$W^+ \to e^+\nu$	$W^- \to e^-\bar{\nu}$
Electron Trigger	–	–	–	0.5	3.0	3.2
Electron Reconstruction, Identification	–	–	–	3.8	2.0	2.1
Electron Isolation	–	–	–	1.0	0.5	0.5
Electron Scale and Resolution	–	–	–	0.2	0.4	0.5
Charge Identification	–	–	–	0.8	0.1	0.1
Muon Trigger	1.0	2.0	2.0	–	–	–
Muon Reconstruction, Identification	0.9	0.4	0.4	–	–	–
Muon Isolation	0.5	0.3	0.3	–	–	–
Muon Scale and Resolution	0.1	0.1	0.1	–	–	–
JES and JER	–	1.5	1.5	–	1.9	1.8
MET Soft Term	–	0.1	0.1	–	0.1	0.1
Pileup Modeling	0.9	1.2	1.2	0.9	1.4	1.4
Total	1.7	2.8	2.8	4.1	4.4	4.5

Table 8: Systematic uncertainties given in percent on C-factors for Z and $W^\pm$ boson production measurements in different channels.

- **Charge Identification:** About 0.7% of electrons have their charge reconstructed wrongly, primarily because of showering and photon conversions in the inner detector material. This effect is studied using $Z \to ee$ events in which both electrons are reconstructed with the same charge and found to be well described by the Monte Carlo simulation, within the statistical uncertainty of the control sample. An uncertainty is assessed to cover the small residual differences between data and simulation. The charge mis-reconstruction probability for muons is negligible.

Uncertainties specific to the muon channel are:

- **Trigger:** The trigger efficiency in simulated events is corrected with scale factors to match that measured in the data. The trigger scale factor uncertainty is the largest uncertainty for the $W \to \mu\nu$ and the $Z \to \mu\mu$ channel.

- **Identification and Reconstruction:** The efficiencies of the muon offline selection (reconstruction/identification and isolation) are corrected with data-driven scale factors.

- **Momentum Scale and Resolution:** The uncertainties on the muon momentum calibration give a small change of acceptance because of migration of events below and above the p_T threshold and across the $m_{\ell\ell}$ boundaries in the $Z \to \ell^+\ell^-$ channels.

Uncertainties common to the electron and the muon channel are as follows:

- **Jet Energy scale and Resolution:** Jets with calibrated p_T above 20 GeV that pass the jet-vertex-tagger algorithm requirements are considered as hard objects in the calculation of the E_T^{miss}, and the corresponding uncertainties on the energy calibration and resolution are propagated to their energies.

- E_T^{miss} **scale and Resolution:** Several possible sources of uncertainty on the soft component of the E_T^{miss} scale and resolution have been considered [40] but they result in estimated uncertainties below the percent level.

- **Pileup**: The imperfect modelling of the underlying event and pile-up effects leads to acceptance changes at the level of $\pm 1\%$ for C_W and C_Z .
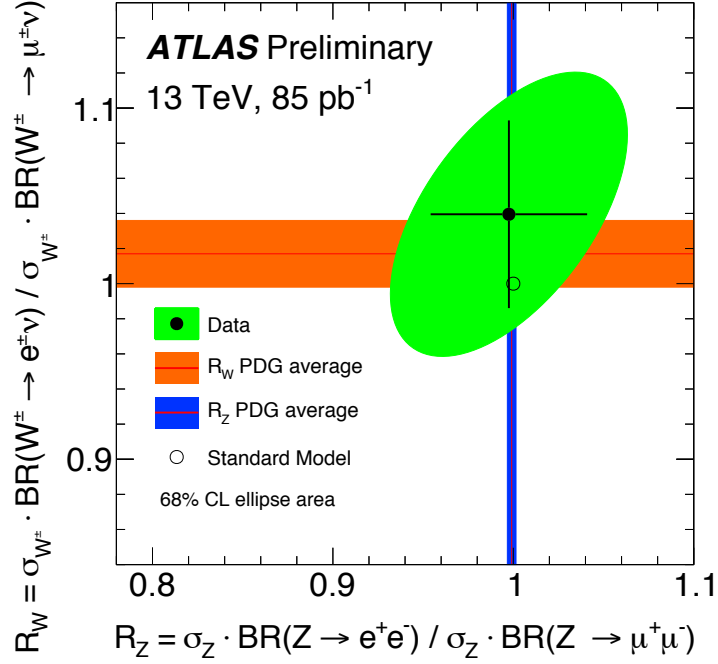
Figure 17: Ratio of the electron- and muon-channel measurements of the Z and $W^\pm$-boson production fiducial cross sections, compared to the expectations of the Standard Model and previous experimental checks of lepton universality shown as PDG average bands.

8.2 Cross-section measurement

All of the elements necessary to calculate the fiducial and total cross sections for W^+, W^- and Z boson production and decay in the electron and muon channels are summarised in Tables 9 and 10. The derived fiducial and total cross sections are also presented in this table, along with their statistical, systematic, and luminosity uncertainties.

The results obtained in the electron and muon channels are expected to agree, following lepton universality in $W^\pm$ and Z boson decays, which has been probed with high accuracy at LEP [42] and by the ATLAS, CDF and D0 experiments [15, 43, 44]. The ratios of the fiducial electron and muon channel measurements in the $W^\pm$ ($R_{W^\pm}$) and the Z (R_Z) boson channels, calculated taking into account correlated systematic uncertainties, are shown in Figure 17. Within uncertainties, the ratios agree with the Standard Model expectations.

Since the cross-section results in the two channels agree well, they are combined, taking into account correlated systematic uncertainties. The combination is performed for the W^+, W^- and Z boson fiducial cross sections simultaneously using the HERAverager program [45, 46]. The combination uses individual sources of the systematic uncertainties, as shown in Table 8. Sources corresponding to lepton reconstruction and identification are naturally uncorrelated between the electron and muon channels. Other sources may affect $W^\pm$ boson measurements only, *e.g.* those which affect missing E_T reconstruction. The multijet background is treated as uncorrelated between the $W^\pm$ boson charges and channels. The common normalization uncertainty due to the luminosity calibration is excluded from the combination procedure and applied separately to the result.

	W^+	W^-
	Electron channel	
	value ± stat ± syst ± lumi	value ± stat ± syst ± lumi
Background-subtracted signal	$231600 \pm 500 \pm 6700 \pm 900$	$181600 \pm 500 \pm 6900 \pm 800$
Correction C_W	0.610 ± 0.028	0.623 ± 0.027
Fiducial cross section (pb)	$4490 \pm 10 \pm 240 \pm 420$	$3442 \pm 9 \pm 200 \pm 324$
Acceptance A_W	0.396 ± 0.010	0.399 ± 0.010
Total cross section (pb)	$11330 \pm 30^{+680}_{-670} \pm 1070$	$8630 \pm 20^{+540}_{-550} \pm 810$
	Muon channel	
	value ± stat ± syst ± lumi	value ± stat ± syst ± lumi
Background-subtracted signal	$240300 \pm 500 \pm 3600 \pm 1780$	$184500 \pm 500 \pm 3200 \pm 1587$
Correction C_W	$0.660^{+0.019}_{-0.020}$	0.656 ± 0.020
Fiducial cross section (pb)	$4304 \pm 9^{+140}_{-145} \pm 419$	$3325 \pm 8^{+113}_{-115} \pm 328$
Acceptance A_W	0.396 ± 0.010	0.399 ± 0.010
Total cross section (pb)	$10870 \pm 20^{+450}_{-460} \pm 1060$	$8330 \pm 20 \pm 360 \pm 820$

Table 9: Results for the fiducial cross sections $\sigma^{\mathrm{fid}}_{W^\pm}$ and total cross section $\sigma^{\mathrm{tot}}_{W^\pm}$ for W^+ and W^- in the electron and muon channels. The observed numbers of signal events after background subtraction are shown for each channel, along with the correction factors C_W, the fiducial cross sections, the geometrical acceptance correction factors A_W, and the total cross sections. Each value is given with statistical, systematic, and luminosity uncertainties quoted in that order. The correction factors are given with a total uncertainty only.

The combination yields a good $\chi^2/N_{\mathrm{d.o.f.}} = 0.9/3$, indicating excellent compatibility of the measurements. Table 11 gives the resulting combined cross sections. There is a sizable reduction of uncertainty compared to individual electron and muon channel measurements since most of the systematic error sources are uncorrelated. Table 12 reports the correlation coefficients among the fiducial cross-section measurements, excluding the correlation due to luminosity uncertainty. As expected, there is a large correlation between W^+ and W^- boson results.

The combined fiducial cross sections are extrapolated to the full phase space using the A_W and A_Z factors, which are given in Tables 9 and 10. The resulting combined total cross sections are given in Table 13.

The combined fiducial and total cross sections are compared in Figures 18 and 19 to the predictions which are calculated using different PDF sets. The measurements agree well with the predictions. The measurement experimental precision is already comparable to PDF uncertainties; however, the experimental precision is diluted by the uncertainty of the preliminary luminosity calibration.

In Figures 20 and 21, the combined electron and muon total cross-section measurements at $\sqrt{s} = 13$ TeV are compared to the theoretical predictions and to previous measurements of the total $W^\pm$ and Z boson production cross sections by: ATLAS [15] and CMS [47, 48], the UA1 [49] and UA2 [50] experiments at

	Z	
	Electron channel	**Muon channel**
	value ± stat ± syst ± lumi	value ± stat ± syst ± lumi
Background-subtracted signal	$34730 \pm 190 \pm 20$	$44600 \pm 210 \pm 30$
Correction C_Z	0.552 ± 0.023	$0.708 ^{+0.012}_{-0.013}$
Fiducial cross section [pb]	$742 \pm 4 \pm 31 \pm 67$	$744 \pm 4 \pm 13 \pm 67$
Acceptance A_Z	0.399 ± 0.006	0.399 ± 0.006
Total cross section [pb]	$1861 \pm 10 \pm 82 \pm 167$	$1865 \pm 9 \pm 43 \pm 168$

Table 10: Results for the fiducial cross sections σ_Z^{fid} and total cross section σ_Z^{tot} for Z in the electron and muon channels. The observed numbers of signal events after background subtraction are shown for each channel, along with the correction factors C_Z, the fiducial cross sections, the geometrical acceptance correction factors A_Z, and the total cross sections with their statistical, systematic, and luminosity uncertainties quoted in that order. The correction factors are given with a total uncertainty only.

Channel	value ± stat ± syst ± lumi [pb]
W^-	$3344 \pm 6 \pm 113 \pm 301$
W^+	$4340 \pm 7 \pm 138 \pm 391$
$W^\pm$	$7684 \pm 9 \pm 232 \pm 692$
Z	$746 \pm 3 \pm 13 \pm 67$

Table 11: Results for the fiducial cross section σ^{fid} for the combined electron and muon channel W^-, W^+, $W^\pm$, and Z boson production measurements.

	W^-	W^+	Z
W^-	1	0.71	0.20
W^+		1	0.16
Z			1

Table 12: Correlation coefficients among W^-, W^+, and Z boson production combined fiducial cross-section measurements excluding the common normalisation uncertainty due to the luminosity calibration.

$\sqrt{s} = 0.63$ TeV at the CERN Sp$\overline{\text{p}}$S, by the CDF [43] and D0 [51] experiments at $\sqrt{s} = 1.8$ TeV and $\sqrt{s} = 1.96$ TeV at the Fermilab Tevatron colliders, and to the $W^\pm$ boson production cross-section measurement by the PHENIX [52] experiment in proton-proton collisions at $\sqrt{s} = 0.5$ TeV at the RHIC collider. The calculations were performed with the program Fewz using the MSTW2008NNLO parton density function parameterisation [53]. The theoretical predictions are in good agreement with all measurements. The energy dependence of the total $W^\pm$ and Z boson production cross sections is well described.

Channel	value ± stat ± syst ± lumi
	[pb]
W^-	$8380 \pm 20 \pm 350 \pm 750$
W^+	$10960 \pm 20 \pm 440 \pm 990$
$W^\pm$	$19350 \pm 20 \pm 760 \pm 1740$
Z	$1869 \pm 7 \pm 42 \pm 168$

Table 13: Results for the total cross section σ^{tot} for the combined electron and muon channel W^-, W^+, $W^\pm$, and Z boson production measurements.
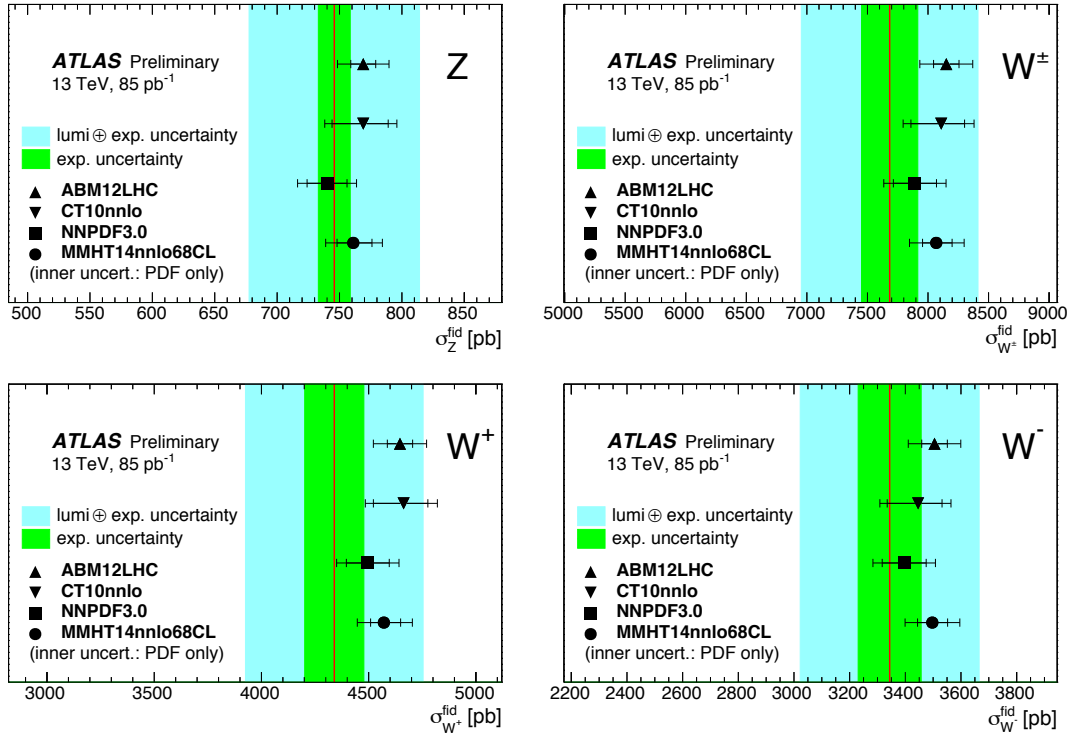
Figure 18: Predictions for the combined fiducial cross sections σ_Z^{fid}, $\sigma_{W^\pm}^{\text{fid}}$, $\sigma_{W^+}^{\text{fid}}$, and $\sigma_{W^-}^{\text{fid}}$ for the four PDFs CT10NNLO, NNPDF3.0, MMHT14NNLO68CL, and ABM12LHC compared to the measured fiducial cross sections (red line) as given in Table 11. The green (cyan) band corresponds to the experimental uncertainty without (with) the luminosity uncertainty. The inner error bar of the predictions represents the PDF uncertainty while the outer error bar includes the sum of all other systematics.
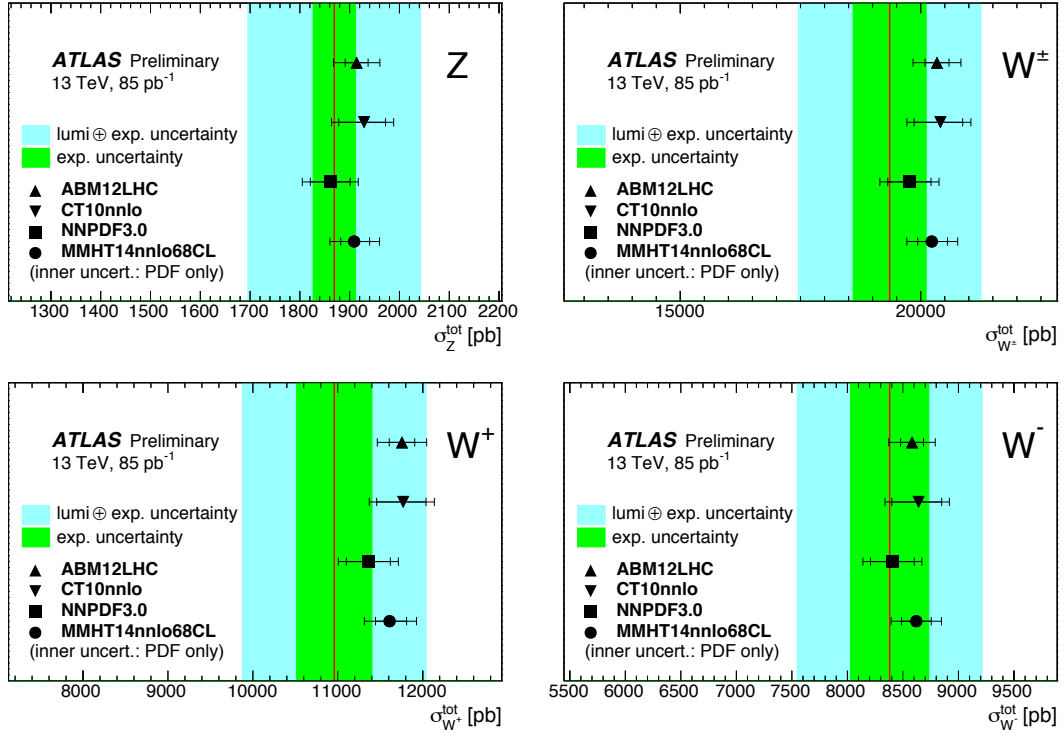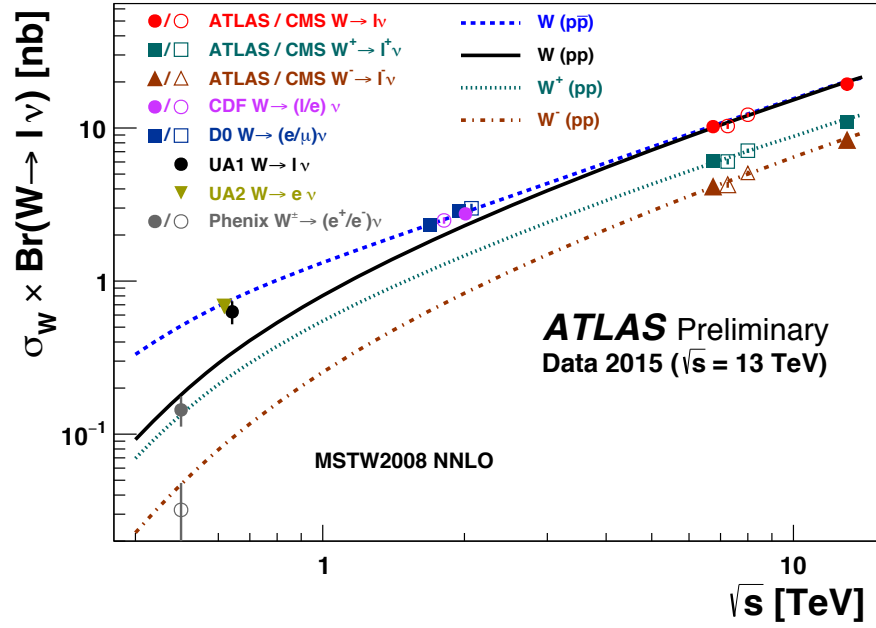
Figure 19: Predictions for the combined total cross sections σ_Z^{tot}, $\sigma_{W^\pm}^{\mathrm{tot}}$, $\sigma_{W^+}^{\mathrm{tot}}$, $\sigma_{W^-}^{\mathrm{tot}}$ for the four PDFs CT10NNLO, NNPDF3.0, MMHT14NNLO68CL, and ABM12LHC compared to the measured total cross sections (red line) as given in Table 13. The green (cyan) band corresponds to the experimental uncertainty without (with) the luminosity uncertainty. The inner error bar of the predictions represents the PDF uncertainty while the outer error bar includes the sum of all other systematics.

Figure 20: The measured values of $\sigma_W \times \mathrm{BR}\,(W \to \ell\nu)$ for W^+, W^- and for their sum compared to the theoretical predictions based on NNLO QCD calculations (see text). Results are shown for the combined electron-muon results. The predictions are shown for both proton-proton (W^+, W^- and their sum) and proton-antiproton colliders ($W^\pm$) as a function of $\sqrt{s}$. In addition, previous measurements at proton-antiproton and proton-proton colliders are shown. The data points at the various energies are staggered to improve readability. The CDF and D0 measurements are shown for both Tevatron collider energies, $\sqrt{s} = 1.8$ TeV and $\sqrt{s} = 1.96$ TeV. All data points are displayed with their total uncertainty. The theoretical uncertainties on the cross-section predictions are not shown.
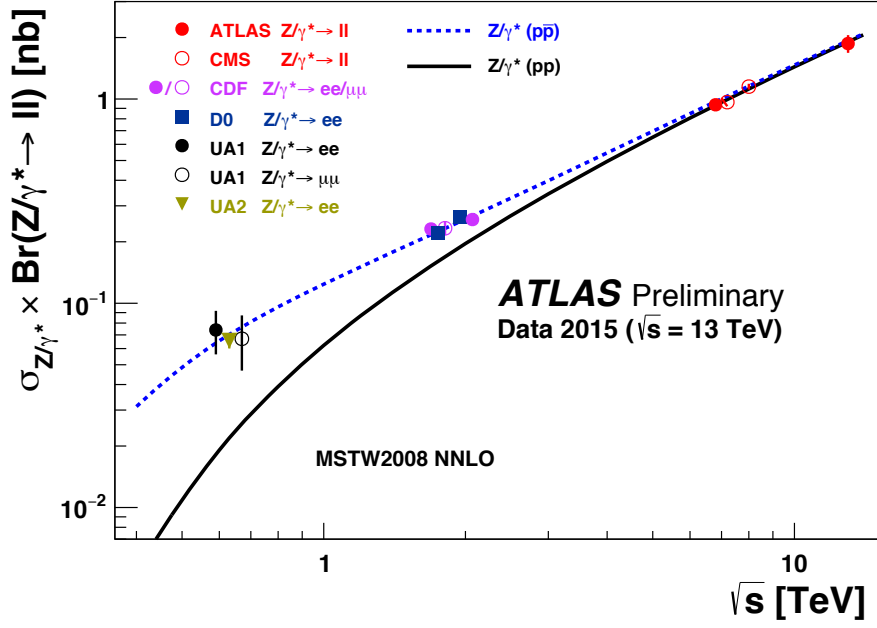
Figure 21: The measured value of $\sigma_{Z/\gamma^*} \times \mathrm{BR}\,(Z/\gamma^* \to \ell^+\ell^-)$ where the electron and muon channels have been combined, compared to the theoretical predictions based on NNLO QCD calculations (see text). The predictions are shown for both proton-proton and proton-antiproton colliders as a function of $\sqrt{s}$. In addition, previous measurements at proton-antiproton colliders are shown. The data points at the various energies are staggered to improve readability. The CDF and D0 measurements are shown for both Tevatron collider energies, $\sqrt{s} = 1.8$ TeV and $\sqrt{s} = 1.96$ TeV. All data points are displayed with their total uncertainty. The theoretical uncertainties on the cross-section predictions are not shown.

8.3 Cross-section ratio measurement

Ratios of the measured cross sections benefit from the cancellation of some experimental uncertainties. The ratios of W^+ to W^- (R_{W^+/W^-}) and $W^\pm$ to Z ($R_{W^\pm/Z}$) boson production were measured by the ATLAS and CMS collaboration in the past [15, 47, 48] and proved to be powerful tools to constrain PDF uncertainties. The ratio of W^+ to W^- boson cross sections is mostly sensitive to the difference of u_v and d_v valence-quark distributions at low Bjorken-x while the ratio of $W^\pm$ to Z boson cross sections constrains the strange-quark distribution. Studies from Ref. [54] show that starting from a precision of about 2%, the measurements at $\sqrt{s}$ = 13 TeV begin to have significant constraining power to PDFs, compared to PDF sets such as CT10 and the recent MMHT14 and NNPDF3.0.

The systematic uncertainties of the cross-section measurements are largely uncorrelated between the electron and muon channels, apart from the common luminosity uncertainty. On the other hand there is a strong correlation between W^+ and W^- boson measurements. There is also significant correlation between the $W^\pm$ and Z boson results for the same flavour measurement.

The results for the ratios of fiducial cross sections for W^+ to W^- boson production and for $W^\pm$ to Z boson production are given in Table 14. The ratios obtained in the electron and muon channels agree well with each other, and the ratio of the combined results has a reduced uncertainty. The ratios of the combined results are compared to theory predictions in Figures 22 and 23. For the ratio $R_{W^+/W^-} = \sigma^{\mathrm{fid}}_{W^+}/\sigma^{\mathrm{fid}}_{W^-}$, there is a significant scatter for different PDF predictions and the accuracy of the experimental result is comparable to the spread among them. The data favours results from the PDFs which include LHC measurements from Run 1 (ABM12, NNPDF3.0 and MMHT14). For the ratio $R_{W/Z} = \sigma^{\mathrm{fid}}_{W^\pm}/\sigma^{\mathrm{fid}}_Z$, the predictions agree within quoted uncertainties and the measurement is consistent with all of them.
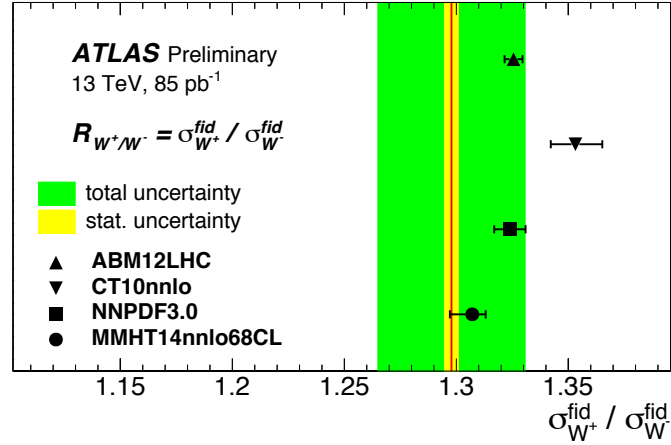

Figure 22: Ratio of W^+ to W^--boson production combined fiducial cross sections (red line) compared to predictions based on different PDF sets. The inner shaded band corresponds to the statistical uncertainty while the outer band shows statistical and systematic uncertainties added in quadrature. The theory predictions are given with the corresponding PDF uncertainties shown as error bars. Scale uncertainties are not included in the error bars of the predictions.

Channel	$\sigma_{W^+}^{\text{fid}}/\sigma_{W^-}^{\text{fid}}$	$\sigma_{W^\pm}^{\text{fid}}/\sigma_Z^{\text{fid}}$
e-channel	$1.304 \pm 0.004 \pm 0.061$	$10.68 \pm 0.06 \pm 0.54$
μ-channel	$1.294 \pm 0.004 \pm 0.038$	$10.25 \pm 0.05 \pm 0.33$
combined	$1.298 \pm 0.003 \pm 0.033$	$10.30 \pm 0.04 \pm 0.33$

Table 14: Ratios of the W^+ to W^- and $W^\pm$ to Z boson fiducial cross sections for the electron, muon and combined measurements. The uncertainties are separated into statistical and systematic uncertainties, in that order.
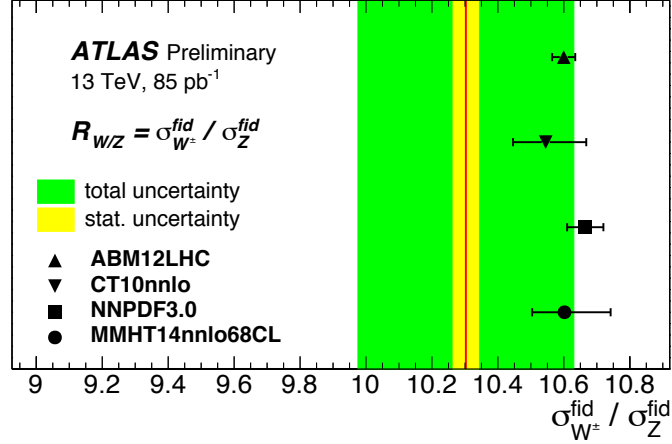

Figure 23: Ratio of $W^\pm$ to Z-boson production combined fiducial cross sections (red line) compared to predictions based on different PDF sets. The inner shaded band corresponds to statistical uncertainty while the outer band shows statistical and systematic uncertainties added in quadrature. The theory predictions are given with the corresponding PDF uncertainties shown as error bars. Scale uncertainties are not included in the error bars of the predictions.

9 Conclusion

Measurements with the ATLAS detector of the $W \to \ell\nu$ and $Z \to \ell^+\ell^-$ production cross sections based on 950153 and 79854 candidates, respectively, are presented in this note. These results, produced from $\sqrt{s} = 13$ TeV proton-proton collisions, correspond to a total integrated luminosity of approximately 85 pb^{-1}. The measured total inclusive $W^\pm$-boson production cross sections times the respective leptonic branching ratios for the combined electron and muon channels are $\sigma_{W^+}^{\text{tot}} = [10960 \pm 20\,(\text{stat}) \pm 440\,(\text{sys}) \pm 990\,(\text{lumi})]$ pb and $\sigma_{W^-}^{\text{tot}} = [8380 \pm 20\,(\text{stat}) \pm 350\,(\text{sys}) \pm 750\,(\text{lumi})]$ pb. The total inclusive Z-boson production cross section times leptonic branching ratio, within the invariant mass window $66 < m_{\ell\ell} < 116$ GeV, is $\sigma_Z^{\text{tot}} = [1869 \pm 7\,(\text{stat}) \pm 42\,(\text{sys}) \pm 168\,(\text{lumi})]$ pb. These results are the first $W^\pm$ and Z production cross sections measured by ATLAS at $\sqrt{s} = 13$ TeV, the highest centre-of-mass energy ever available from a collider, and show agreement with theoretical calculations based on NNLO QCD. The measurements of cross-section ratios benefit from the cancellation of some experimental uncertainties, and are powerful tools to constrain PDF uncertainties. In particular, the cross-section ratio of W^+ to W^- is measured at the 2.5% level.

References

[1] ATLAS Collaboration, *The ATLAS Experiment at the CERN Large Hadron Collider*, JINST **3** (2008) S08003.

[2] ATLAS Collaboration, *ATLAS Insertable B-Layer Technical Design Report*, CERN-LHCC-2010-013. ATLAS-TDR-19, 2010, URL: http://cds.cern.ch/record/1291633.

[3] K. Melnikov and F. Petriello, *Electroweak gauge boson production at hadron colliders through $O(\alpha_s^2)$*, Phys. Rev. D **74** (2006) 114017, arXiv: hep-ph/0609070 [hep-ph].

[4] R. Gavin et al., *FEWZ 2.0: A code for hadronic Z production at next-to-next-to-leading order*, Comput. Phys. Commun. **182** (2011) 2388, arXiv: 1011.3540 [hep-ph].

[5] R. Gavin et al., *W Physics at the LHC with FEWZ 2.1*, Comput. Phys. Commun. **184** (2013) 208, arXiv: 1201.5896 [hep-ph].

[6] Y. Li and F. Petriello, *Combining QCD and electroweak corrections to dilepton production in FEWZ*, Phys. Rev. D **86** (2012) 094034, arXiv: 1208.5967 [hep-ph].

[7] J. Gao et al., *CT10 next-to-next-to-leading order global analysis of QCD*, Phys. Rev. **D89** (2014) 033009, arXiv: 1302.6246 [hep-ph].

[8] R. D. Ball et al., *Parton distributions for the LHC Run II*, JHEP **04** (2015) 040, arXiv: 1410.8849 [hep-ph].

[9] L. A. Harland-Lang et al., *Parton distributions in the LHC era: MMHT 2014 PDFs*, Eur. Phys. J. **C75** (2015) 204, arXiv: 1412.3989 [hep-ph].

[10] S. Alekhin, J. Bluemlein and S. Moch, *The ABM parton distributions tuned to LHC data*, Phys. Rev. **D89** (2014) 054028, arXiv: 1310.3059 [hep-ph].

[11] P. Nason, *A New method for combining NLO QCD with shower Monte Carlo algorithms*, JHEP **11** (2004) 040, arXiv: hep-ph/0409146 [hep-ph].

[12] S. Frixione, P. Nason and C. Oleari, *Matching NLO QCD computations with Parton Shower simulations: the POWHEG method*, JHEP **11** (2007) 070, arXiv: 0709.2092 [hep-ph].

[13] S. Alioli et al., *A general framework for implementing NLO calculations in shower Monte Carlo programs: the POWHEG BOX*, JHEP **06** (2010) 043, arXiv: 1002.2581 [hep-ph].

[14] T. Sjostrand, S. Mrenna and P. Z. Skands, *A Brief Introduction to PYTHIA 8.1*, Comput. Phys. Commun. **178** (2008) 852–867, arXiv: 0710.3820 [hep-ph].

[15] ATLAS Collaboration, *Measurement of the inclusive $W^{\pm}$ and Z/gamma cross sections in the electron and muon decay channels in pp collisions at $\sqrt{s}$ = 7 TeV with the ATLAS detector*, Phys. Rev. **D85** (2012) 072004, arXiv: 1109.5141 [hep-ex].

[16] D. Bardin et al., *SANC integrator in the progress: QCD and EW contributions*, JETP Lett. **96** (2012) 285–289, arXiv: 1207.4400 [hep-ph].

[17] A. B. Arbuzov, R. R. Sadykov and Z. Was, *QED Bremsstrahlung in decays of electroweak bosons*, Eur. Phys. J. **C73**.11 (2013) 2625, arXiv: 1212.6783 [hep-ph].

[18] W. F. L. Hollik, *Radiative Corrections in the Standard Model and their Role for Precision Tests of the Electroweak Theory*, Fortsch. Phys. **38** (1990) 165–260.

[19] S. Dittmaier and M. Huber, *Radiative corrections to the neutral-current Drell-Yan process in the Standard Model and its minimal supersymmetric extension*, JHEP **01** (2010) 060, arXiv: 0911.2329 [hep-ph].

[20] N. Davidson, T. Przedzinski and Z. Was, *PHOTOS Interface in C++: Technical and Physics Documentation* (2010), arXiv: 1011.0937 [hep-ph].

[21] ATLAS Collaboration, *Simultaneous measurements of the $t\bar{t}$, W^+W^-, and $Z/\gamma^* \to \tau\tau$ production cross-sections in pp collisions at $\sqrt{s}$ = 7 TeV with the ATLAS detector*, Phys. Rev. D **91** (2015) 052005, arXiv: 1407.0573 [hep-ex].

[22] ATLAS Collaboration, *Improved luminosity determination in pp collisions at $\sqrt{s}$ = 7 TeV using the ATLAS detector at the LHC*, Eur. Phys. J. C **73** (2013) 2518, arXiv: 1302.4393 [hep-ex].

[23] S. Alioli et al., *NLO vector-boson production matched with shower in POWHEG*, JHEP **0807** (2008) 060, arXiv: 0805.4802 [hep-ph].

[24] H.-L. Lai et al., *New parton distributions for collider physics*, Phys. Rev. **D82** (2010) 074024, arXiv: 1007.2241 [hep-ph].

[25] ATLAS Collaboration, *Measurement of the Z/γ^* boson transverse momentum distribution in pp collisions at $\sqrt{s}$ = 7 TeV with the ATLAS detector*, JHEP **1409** (2014) 145, arXiv: 1406.3660 [hep-ex].

[26] D. J. Lange, *The EvtGen particle decay simulation package*, Nucl. Instrum. Meth. **A462** (2001) 152.

[27] T. Sjostrand, S. Mrenna and P. Z. Skands, *PYTHIA 6.4 Physics and Manual*, JHEP **05** (2006) 026, arXiv: hep-ph/0603175 [hep-ph].

[28] M. Czakon and A. Mitov, *Top++: A Program for the Calculation of the Top-Pair Cross-Section at Hadron Colliders*, Comput. Phys. Commun. **185** (2014) 2930, arXiv: 1112.5675 [hep-ph].

[29] T. Gleisberg et al., *Event generation with SHERPA 1.1*, JHEP **02** (2009) 007, arXiv: 0811.4622 [hep-ph].

[30] T. Gleisberg and S. Höche, *Comix, a new matrix element generator*, JHEP **0812** (2008) 039, arXiv: 0808.3674 [hep-ph].

[31] F. Cascioli, P. Maierhofer and S. Pozzorini, *Scattering Amplitudes with Open Loops*, Phys. Rev. Lett. **108** (2012) 111601, arXiv: 1111.5206 [hep-ph].

[32] S. Schumann and F. Krauss, *A Parton shower algorithm based on Catani-Seymour dipole factorisation*, JHEP **0803** (2008) 038, arXiv: 0709.1027 [hep-ph].

[33] S. Höche et al., *QCD matrix elements + parton showers: The NLO case*, JHEP **04** (2013) 027, arXiv: 1207.5030 [hep-ph].

[34] ATLAS Collaboration, *Summary of ATLAS Pythia 8 tunes*, ATLAS-PHYS-PUB-2012-003, 2012, URL: http://cdsweb.cern.ch/record/1474107.

[35] S. Agostinelli et al., *GEANT4: A Simulation toolkit*, Nucl. Instrum. Meth. **A506** (2003) 250–303.

[36] ATLAS Collaboration, *The ATLAS Simulation Infrastructure*, Eur. Phys. J. C **70** (2010) 823, arXiv: `1005.4568 [hep-ex]`.

[37] ATLAS Collaboration, *Electron efficiency measurements with the ATLAS detector using the 2012 LHC proton-proton collision data*, ATLAS-CONF-2014-032, 2014, URL: `https://cds.cern.ch/record/1706245`.

[38] ATLAS Collaboration, *Muon reconstruction performance in early Run II*, ATL-PHYS-PUB-2015-037, 2015, URL: `https://atlas.web.cern.ch/Atlas/GROUPS/PHYSICS/PUBNOTES/ATL-PHYS-PUB-2015-037`.

[39] M. Cacciari, G. P. Salam and G. Soyez, *The anti-kt jet clustering algorithm*, JHEP **0804** (2008) 063, arXiv: `0802.1189 [hep-ph]`.

[40] ATLAS Collaboration, *Jet Calibration and Systematic Uncertainties for Jets Reconstructed in the ATLAS Detector at $\sqrt{s}$ = 13 TeV*, ATL-PHYS-PUB-2015-015, 2015, URL: `https://cds.cern.ch/record/2028594`.

[41] ATLAS Collaboration, *Tagging and suppression of pileup jets with the ATLAS detector*, ATLAS-CONF-2014-018, 2014, URL: `https://cds.cern.ch/record/1700870`.

[42] S. Schael et al., *Precision electroweak measurements on the Z resonance*, Phys. Rept. **427** (2006) 257–454, arXiv: `hep-ex/0509008 [hep-ex]`.

[43] A. Abulencia et al., *Measurements of inclusive W and Z cross sections in p anti-p collisions at $\sqrt{s}$ = 1.96-TeV*, J. Phys. **G34** (2007) 2457–2544, arXiv: `hep-ex/0508029 [hep-ex]`.

[44] S. Abachi et al., *W and Z boson production in $p\bar{p}$ collisions at $\sqrt{s}$ = 1.8-TeV*, Phys. Rev. Lett. **75** (1995) 1456–1461, arXiv: `hep-ex/9505013 [hep-ex]`.

[45] A. Glazov, *Averaging of DIS cross section data*, AIP Conf. Proc. **792** (2005) 237–240.

[46] F. D. Aaron et al., *Measurement of the Inclusive ep Scattering Cross Section at Low Q^2 and x at HERA*, Eur. Phys. J. **C63** (2009) 625–678, arXiv: `0904.0929 [hep-ex]`.

[47] CMS Collaboration, *Measurement of the Inclusive W and Z Production Cross Sections in pp Collisions at $\sqrt{s}$ = 7 TeV*, JHEP **10** (2011) 132, arXiv: `1107.4789 [hep-ex]`.

[48] CMS Collaboration, *Measurement of inclusive W and Z boson production cross sections in pp collisions at $\sqrt{s}$ = 8 TeV*, Phys. Rev. Lett. **112** (2014) 191802, arXiv: `1402.0923 [hep-ex]`.

[49] C. Albajar et al., *Intermediate Vector Boson Cross-Sections at the CERN Super Proton Synchrotron Collider and the Number of Neutrino Types*, Phys. Lett. **B198** (1987) 271.

[50] J. Alitti et al., *A Measurement of the W and Z production cross-sections and a determination of Gamma (W) at the CERN $\bar{p}p$ collider*, Phys. Lett. **B276** (1992) 365–374.

[51] D0 Collaboration. *Measurement of the Cross Section for W and Z Production to Electron Final States with the D0 detector at $\sqrt{s}$=1.96 TeV and Measurement of the Cross-section Production in the Muon Channel at $\sqrt{s}$=1.96 TeV Using the D0 Detector*, D0 conference notes: 4403-CONF, 4750-CONF, `http://www-d0.fnal.gov/Run2Physics/WWW/results/prelim/EW/E06/E06.pdf`.

[52] A. Adare et al., *Cross Section and Parity Violating Spin Asymmetries of $W^{\pm}$ Boson Production in Polarized p + p Collisions at $\sqrt{s}$ = 500 GeV*, Phys. Rev. Lett. **106** (2011) 062001, arXiv: `1009.0505 [hep-ex]`.

[53] A. D. Martin et al., *Parton distributions for the LHC*, Eur. Phys. J. **C63** (2009) 189–285, arXiv: `0901.0002 [hep-ph]`.

[54] J. Rojo et al.,
The PDF4LHC report on PDFs and LHC data: Results from Run I and preparation for Run II
(2015), arXiv: `1507.00556 [hep-ph]`.